Saturn's Tropospheric Composition and Clouds from Cassini/VIMS 4.6-5.1 m Nightside Spectroscopy

Leigh N. Fletcher, Kevin H. Baines, Thomas W. Momary, Adam P. Showman, Patrick G.J. Irwin, Glenn S. Orton, Maarten Roos-Serote, C. Merlet

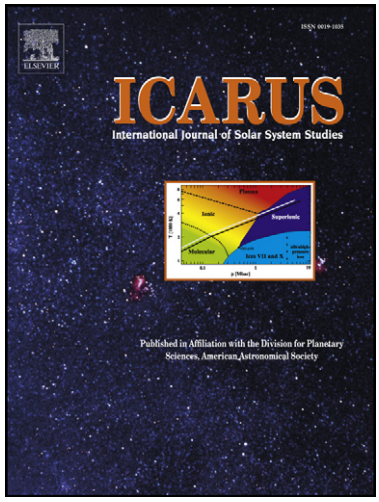

Saturn's Tropospheric Composition and Clouds from Cassini/VIMS 4.6-5.1 μm Nightside Spectroscopy

Leigh N. Fletcher, Kevin H. Baines, Thomas W. Momary, Adam P. Showman, Patrick G.J. Irwin, Glenn S. Orton, Maarten Roos-Serote, C. Merlet

PII: S0019-1035(11)00215-6
DOI: 10.1016/j.icarus.2011.06.006
Reference: YICAR 9849

To appear in: *Icarus*

Received Date: 28 February 2011
Revised Date: 1 June 2011
Accepted Date: 6 June 2011

Please cite this article as: Fletcher, L.N., Baines, K.H., Momary, T.W., Showman, A.P., Irwin, P.G.J., Orton, G.S., Roos-Serote, M., Merlet, C., Saturn's Tropospheric Composition and Clouds from Cassini/VIMS 4.6-5.1 μm Nightside Spectroscopy, *Icarus* (2011), doi: 10.1016/j.icarus.2011.06.006

Saturn′s Tropospheric Composition and Clouds from Cassini/VIMS 4.6-5.1 μm Nightside Spectroscopy

Leigh N. Fletcher[a], Kevin H. Baines[b], Thomas W. Momary[c], Adam P. Showman[d], Patrick G.J. Irwin[a], Glenn S. Orton[c], Maarten Roos-Serote[e], C. Merlet[a]

[a]*Atmospheric, Oceanic & Planetary Physics, Department of Physics, University of Oxford, Clarendon Laboratory, Parks Road, Oxford, OX1 3PU, UK*
[b]*SSEC, University of Wisconsin-Madison, 1225 W. Dayton Street, Madison, Wisconsin, 53706, USA*
[c]*Jet Propulsion Laboratory, California Institute of Technology, 4800 Oak Grove Drive, Pasadena, CA, 91109, USA*
[d]*Department of Planetary Sciences, Lunar and Planetary Laboratory, University of Arizona, Tucson, AZ 85721, USA*
[e]*Lisbon Astronomical Observatory, Tapada da Ajuda, 1349-018 Lisbon, Portugal*

Abstract

The latitudinal variation of Saturn's tropospheric composition (NH_3, PH_3 and AsH_3) and aerosol properties (cloud altitudes and opacities) are derived from Cassini/VIMS 4.6-5.1 μm thermal emission spectroscopy on the planet's nightside (April 22, 2006). The gaseous and aerosol distributions are used to trace atmospheric circulation and chemistry within and below Saturn's cloud decks (in the 1- to 4-bar region). Extensive testing of VIMS spectral models is used to assess and minimise the effects of degeneracies between retrieved variables and sensitivity to the choice of aerosol properties. Best fits indicate cloud opacity in two regimes: (a) a compact cloud deck centred in the 2.5-2.8 bar region, symmetric between the northern and southern hemispheres, with small-scale opacity

Email address: fletcher@atm.ox.ac.uk (Leigh N. Fletcher)

variations responsible for numerous narrow light/dark axisymmetric lanes; and (b) a hemispherically asymmetric population of aerosols at pressures less than 1.4 bar (whose exact altitude and vertical structure is not constrained by nightside spectra) which is 1.5 – 2.0× more opaque in the summer hemisphere than in the north and shows an equatorial maximum between ±10° (planetocentric).

Saturn's NH_3 spatial variability shows significant enhancement by vertical advection within ±5° of the equator and in axisymmetric bands at 23-25°S and 42-47°N. The latter is consistent with extratropical upwelling in a dark band on the poleward side of the prograde jet at 41°N (planetocentric). PH_3 dominates the morphology of the VIMS spectrum, and high-altitude PH_3 at $p < 1.3$ bar has an equatorial maximum and a mid-latitude asymmetry (elevated in the summer hemisphere), whereas deep PH_3 is latitudinally-uniform with off-equatorial maxima near ±10°. The spatial distribution of AsH_3 shows similar off-equatorial maxima at ±7° with a global abundance of 2-3 ppb. VIMS appears to be sensitive to both (i) an upper tropospheric circulation (sensed by NH_3 and upper-tropospheric PH_3 and hazes) and (ii) a lower tropospheric circulation (sensed by deep PH_3, AsH_3 and the lower cloud deck).

Keywords: Saturn, Atmospheres, composition, Atmospheres, structure

1. Introduction

The Visual and Infrared Mapping Spectrometer (VIMS, Brown et al., 2004) onboard the Cassini spacecraft exploits a unique region of Saturn's spectrum between 4.6 and 5.1 μm where the effects of scattered sunlight diminish; the collision-induced opacity due to H_2-He is at a minimum and strong CH_4 absorptions are absent. As a result, this wavelength range allows Cassini to probe deeper

into Saturn's troposphere than at any other infrared wavelength. As on Jupiter, this 5-μm window is sensitive to the emission of the gas giant's internal heat, attenuated by overlying cloud decks that appear in silhouette against the warm thermal emission. To date, analysis of VIMS data has focussed on the detailed morphology of images at discrete near-IR wavelengths (e.g., Baines et al., 2006; Baines et al., 2009; Choi et al., 2009), which has revealed a wealth of information about dynamical phenomena within Saturn's cloud decks (e.g., strings of pearls, ribbon waves, the hexagon, polar vortices, annular clouds, and equatorial plumes; see the review by Del Genio et al., 2009). However, the wavelength dependence of Saturn's 4.6-5.1 μm spectrum (1950-2220 cm $^{-1}$) has yet to be fully exploited. In this paper, we study the influences of gaseous distributions and cloud properties on nightside VIMS spectra (i.e., sensitive to thermal emission alone, in the absence of reflected sunlight) to determine the latitudinal distribution of opacity sources in Saturn's troposphere.

Saturn's 5-μm window is expected to be similar to Jupiter's, albeit with a different vertical distribution of tropospheric aerosols due to Saturn's lower gravity. Voyager/IRIS and Galileo/NIMS investigations demonstrated that Jupiter's 5-μm emission was anticorrelated with both the visible albedo and with a variable opacity cloud in the 1-2 bar region (e.g., Westphal et al., 1974; Terrile and Westphal, 1977; Marten et al., 1981; Bezard et al., 1983; Irwin et al., 1998; Roos-Serote et al., 1998; Irwin and Dyudina, 2002). This correlation is not readily apparent on Saturn, where the visible belt/zone contrasts are subdued by the upper tropospheric hazes. Nevertheless, VIMS 5-μm images show extremely detailed zonal organisation, with a diverse range of meteorological features (fine-scale zonal lanes, small vortices and other turbulent structures), some of which

are common to both visible and 5-μm imaging (e.g., Choi et al., 2009; Vasavada et al., 2006).

Orton et al. (2009) reviewed the first investigations of Saturn's 5-μm window from ground-based and space-based platforms, starting with the first spectroscopic detections of CH_3D (Fink and Larson, 1978) and phosphine (PH_3) by Larson (1980) from the Kuiper Airborne Observatory. PH_3 was found to dominate the shape of Saturn's 5-μm emission, but its poorly understood absorption coefficients hampered quantitative analyses of the 5-μm window for many years (Noll and Larson, 1990). The abundance of PH_3 has since been studied at 5 μm using a range of techniques (Bézard et al., 1989; Noll and Larson, 1990; de Graauw et al., 1997). Ground-based observations began to reveal the other principal contributors to the 5-μm spectrum: CO was first detected in UK Infrared Telescope measurements (UKIRT) at 5 μm by Noll et al. (1986); germane (GeH_3) from UKIRT (Noll et al., 1988) and later ISO de Graauw et al. (1997); and arsine (AsH_3) from UKIRT (Noll et al., 1989) and the Canada-France-Hawaii Telescope (Bézard et al., 1989). NH_3 bands ($2\nu_2$ and ν_4) affect the long-wavelength edge of this window and were first detected by Fink et al. (1983), and later refined by Voyager/IRIS (Courtin et al., 1984) and ISO (de Graauw et al., 1997). Detection of a subsolar H_2O distribution at 5-μm had to wait for disc-averaged ISO spectra in the 1990s (de Graauw et al., 1997). Finally, IRTF imaging at 5.1 μm indicated that Saturn's deep cloud layers were spatially inhomogeneous (Yanamandra-Fisher et al., 2001) before Cassini's arrival. Although the spectral resolution of VIMS is necessarily smaller than ground-based instruments, it offers the capability to map the spatial distribution of some of these gases for the first time, without having to correct for telluric contamination.

Besides the wide ranging spectral effects of PH_3, Saturn's poorly-understood cloud properties further complicate quantitative analyses of the VIMS spectra. The expected condensation altitudes for volatiles can be estimated using thermochemical equilibrium theory and knowledge of bulk elemental abundances (Weidenschilling and Lewis, 1973; Atreya et al., 1999), although these do not account for mixing via atmospheric motions. Assuming a five-fold enhancement in concentrations over solar composition, calculations by Atreya et al. (1999) suggested that VIMS observations probe vertical dynamics and chemistry in the NH_3 (base at 2 bar) and NH_4SH (base at 6 bar) ice cloud-forming regions of Saturn's troposphere. Our present knowledge of Saturn's clouds, largely derived from visible and near-IR reflectivity studies, is reviewed by West et al. (2009). Common features of the numerous studies (e.g., Karkoschka and Tomasko, 1992, 1993; Stam et al., 2001; Temma et al., 2005; Pérez-Hoyos et al., 2005; Karkoschka and Tomasko, 2005) include (a) a stratospheric haze ($1 < p < 90$ mbar) of small radius ($r \approx 0.1 - 0.2\mu$m) particles, presumably originating from photochemical processes; (b) a tropospheric haze from the tropopause down to the first condensation cloud deck at 1.5-2.0 bar, possibly with aerosol-free gaps in the vertical distribution; and (c) a possible thick NH_3 cloud, although no spectroscopic signature for NH_3 ice has been observed. As we shall demonstrate in Section 4, VIMS is sensitive to a combination of these upper level ubiquitous hazes and the deeper cloud decks.

The spatial distribution of NH_3 gas is intimately tied to the latitudinal variability of the hazes. Global constraints on the NH_3 vertical distribution have been provided by a number of authors, as highlighted in Table 1. Generally, NH_3 was found to be around 500 ppm below 3 bar (de Pater and Massie, 1985; Briggs

and Sackett, 1989), decreasing to 100 ppm at the condensation altitude (Briggs and Sackett, 1989; Grossman et al., 1989; de Graauw et al., 1997; Orton et al., 2000; Burgdorf et al., 2004) and then decreasing with altitude according to a sub-saturated vapour pressure profile and photolysis in the upper troposphere (e.g., de Graauw et al., 1997; Kerola et al., 1997; Kim et al., 2006; Fletcher et al., 2009b). In this work we derive the latitudinal distribution of gaseous composition (NH_3, PH_3, AsH_3) and cloud opacity (tropospheric clouds and hazes) from VIMS observations of the 5-μm window. Section 2 describes the selection and error sources in the VIMS data; Section 3 introduces the spectral model, techniques and opacity sources allowing us to retrieve atmospheric properties. The degeneracies between assumed cloud distributions and properties is explored in Section 4. Section 5 presents the VIMS-derived distributions of gases and clouds and Section 6 describes their implications for Saturn's tropospheric dynamics and chemistry.

2. Observations

2.1. VIMS Data and Calibration

Saturn's emitted radiance in the 4.6-5.1 μm region is measured by the Visible and Infrared Mapping Spectrometer (VIMS, Brown et al., 2004) on the Cassini spacecraft. Although this instrument actually consists of two bore-sighted grating spectrometers, only the infrared channel (0.85-5.1 μm) is considered in the present study. VIMS has a passively cooled linear array of 256 InSb photodiode detectors operating at 55-60 K. VIMS-IR records spectral images by stepping a 2-axis scan mirror orthogonally in the along-slit (64 pixel positions of the visible channel slit) and cross-dispersion directions. One spectrum is acquired at each of 64 mirror steps in the cross-dispersion direction, yielding an effective pixel size of 0.5 mrad

on a 64×64 pixel grid. The near-IR spectral resolution is approximately 15 nm, sampled at intervals of 16.6 nm.

IR image cubes (two spatial and one spectral dimension) were geometrically and photometrically calibrated (including despiking and flat-fielding with 2005 calibration files) by the VIMS Science team at the University of Arizona. The VIMS calibration procedure was previously described by McCord et al. (2004), although uncertainties in absolute calibration have not been fully documented (Sromovsky and Fry, 2010b). Systematic errors from pre-flight calibration are thought to be as large as 10% in regions of strong telluric H_2O absorption, although random noise is expected to be considerably smaller (less than one digital quantisation number, corresponding to approximately 0.1% of the typical 5-μm radiance). Radiometrically-calibrated VIMS-IR Images were navigated by reconstructing 'backplanes' from the post-observation Cassini Mission SPICE kernels generated by NASA/JPL (i.e., information on latitude and longitude, as well as incidence, emission, azimuthal and phase angles) using the ISIS3 (Integrated Software for Imaging Spectrometers) package provided by USGS (Gaddis et al., 1997).

Artefacts in VIMS spectra identified by Sromovsky and Fry (2010b), particularly those associated with responsivity corrections near overlaps between order sorting filters, are believed to have no effect on the 4.6-5.1 μm spectrum (e.g., Fig. 8 of Brown et al., 2004). Light potentially scattered within the spectrometer has also been identified as a source of enhanced reflectivity in low-signal regions (Sromovsky and Fry, 2010b), although no such discrepancies between data and models have been identified in the 5-μm window. Finally, we found no evidence for a shift in wavelengths from the nominal grid for any of the image cubes used in

this study. Nightside VIMS-IR radiances were assigned uncertainties by considering the larger of (i) 12% of the radiance measured by each pixel, or (ii) 12% of the mean radiance in the 4.6-5.1 μm range. This avoided unequal weightings of retrievals to the low-signal regions of the Saturn spectrum (see Section 3). The 12% envelope is conservative, adding quadrature-estimated errors due to pre-flight calibration as well as forward-model uncertainties on spectral line data. Specifically, we assumed that systematic errors dominate the error budget.

2.2. Data Selection

Reflected sunlight observations of the giant planets are complicated by the uncertain optical properties (shape, size distribution, composition, phase function, opacity) of their cloud and haze layers. To minimise these effects, we considered only VIMS nightside spectra at a sufficient distance from the day/night terminator to ignore scattered sunlight. Scattered sunlight from Saturn's rings is unlikely to contaminate the nightside Saturn spectra, as water ice in the rings has a low albedo at all VIMS wavelengths beyond 2.8 μm, and is particularly dark near 3 and 5 μm (Cuzzi et al., 2009). Thermal emission from the atmosphere, in addition to absorption and scattering processes, should determine the overall shape of the 4.6-5.1 μm spectrum. This study uses eight VIMS-IR image cubes from sequence VIMS_023SA_MIRMAPB010 (part of sequence S20) on April 22, 2006 (Table 2). Saturn subtended 3.1° during these observations, at a distance of 2.2 million km (38 Saturn radii). The relatively large spacecraft range meant that almost the entirety of Saturn was captured within the 32×32 mrad field of view, allowing multiple latitudes to be covered in a single cube (from 40°S to 70°N). Saturn's sub-solar latitude was 17.6°S during these observations (a heliocentric longitude, $L_s = 317.3°$) approaching the southern autumnal equinox. As such,

seasonal hemispheric asymmetries in cloud coloration and atmospheric temperatures (Fletcher et al., 2010) were still present.

The eight VIMS cubes sampled Saturn during an entire 10-hour rotation (Table 2) so that a composite image from these cubes covered 360° of longitude (Fig. 1). The longitudinal displacement of individual features over the 10-hour sequence was not accounted for in the reprojections, and this is particularly apparent in the overlap region of the first and last cubes in Table 2 (120°W). Four wavelengths (4.6 to 5.1 μm) are displayed to demonstrate that atmospheric features appear similar across the spectral range, and that an asymmetry between the northern and southern mid-latitudes persisted in April 2006 (Baines et al., 2006). Indeed, the map at 4.6 μm (Fig. 1d) shows a well-defined boundary at 10°N between the bright north and dark south, and that the equatorial zone is largely indistinguishable from the rest of the southern hemisphere at this wavelength.

The dark equatorial zone is bordered by two regions of diffuse emission between ±5°. This axisymmetric band is colocated with the narrow prograde jet identified by García-Melendo et al. (2010), which exists in addition to the broad equatorial jet. An irregular chain of dark features (referred to as equatorial plumes) impinge on these diffuse regions from both north and south. Mid-latitudes between ±5 − ±32° show the strongest asymmetry between the hemispheres, with the northern hemisphere considerably brighter than the south. Both hemispheres are characterised by a series of latitudinally-narrow bright and dark lanes, similar to those observed in reflected sunlight (Vasavada et al., 2006; Choi et al., 2009). Some discrete features are observed at off-equatorial latitudes (particularly in the bands between 20-30° in both hemispheres), although the spatial resolution of the S20 sequence of images is insufficient to characterise small-scale features such as

the String of Pearls at 33°N (Momary et al., 2006; Choi et al., 2009).

Zonal mean radiances were extracted from the reprojected maps onto two different meridional grids: (i) a coarse grid with a step size and latitude width of 5° for preliminary testing; and (ii) a fine grid with a size and width of 1° for the final zonal profiles. Within each latitude bin, we selected spectra within 10° of the minimum emission angle for the latitude, and restricted selections to phase angles greater than 90° and solar angles greater than 120° - i.e., ensuring that only nightside observations contributed to the average. The hemispheric asymmetry can be clearly seen in the spectral comparison in Fig. 2. Radiances and brightness temperatures for the 4.6-5.1 μm region are compared for five latitudes, showing that the northern mid-latitudes were uniformly 10-12 K brighter than southern mid-latitudes in April 2006. The overall morphology of the spectrum is dominated by absorption from PH_3 gas and tropospheric aerosols, although the band centres for a variety of gases are labelled in Fig. 2b. Note that the broad absorption feature at 4.74 μm is a blend of absorptions due to PH_3, GeH_4, AsH_3 and CO. The unusual 'kink' in the equatorial spectrum at 5.1μm that is absent from other latitudes is a signature of tropospheric NH_3.

3. Spectral Modelling

Fig. 2 showed that VIMS-IR spectra in the 4.6-5.1 μm range are sensitive to a wide variety of gases and aerosols, but that the spectral resolution (approximately 15 nm, or $R = \lambda/\Delta\lambda \approx 330$ at 5 μm) is insufficient to resolve the individual lines. Instead, they blend together into absorption complexes, requiring simultaneous modelling of the entire range to derive the best-fitting atmospheric profile at each latitude. In this section we describe the basic spectral model before exploring the

degeneracies associated with the VIMS spectra in Section 4.

3.1. Reference Atmosphere

Saturn's *a priori* atmospheric structure (temperatures, $T(p)$, and mole fractions, $q(p)$) was defined on a grid of 39 levels equally spaced in log p between 10 mbar and 10 bar. Temperatures at each latitude were obtained from Cassini/CIRS $T(p)$ profiles from Cassini's prime mission (sensitive to the 1-800 mbar range, Fletcher et al., 2010), and extrapolated between 0.8 and 10 bar with a dry adiabatic lapse rate, g/c_p (where g is the latitudinally-variable gravitational acceleration at 1 bar and c_p is the specific heat capacity of Saturn's H_2-He-CH_4 atmosphere).

Collision-induced absorption of H_2-H_2, H_2-He, H_2-CH_4 and CH_4-CH_4 was pre-calculated from the tabulations of Borysow (1991, 1993); Borysow et al. (1988); Borysow and Frommhold (1986, 1987) and references therein. The helium mixing ratio He/H_2 was set to 0.135 (Conrath and Gautier, 2000). Methane and its isotopologues are well-mixed throughout the altitude range of interest, and were included with mole fractions of 4.7×10^{-3} (CH_4); 3.0×10^{-7} (CH_3D) and 5.1×10^{-5} ($^{13}CH_4$) following Fletcher et al. (2009b). The PH_3 profile was set to the CIRS-derived abundance of 6.4 ppm at $p > 0.55$ bar, decreasing due to photolysis at lower pressures with a fractional scale height of 0.27 (the ratio of the PH_3 scale height to the scale height of the bulk atmosphere, Fletcher et al., 2009a). The vertical distribution of NH_3 had a deep mole fraction of 60 ppm (Fletcher et al., 2009b), decreasing with altitude following a saturated vapour pressure profile ($p > 0.3$ bar) and a linear extrapolation to low pressures to represent photolysis ($p < 0.3$ bar). Minor constituents affecting the 4.6-5.1 μm range were assumed to be well-mixed with altitude, and were included with the following mole fractions: CO (1 ppb, Noll and Larson, 1990); GeH_4 (0.4 ppb, Noll and Larson, 1990); AsH_3 (3.0

ppb, Noll and Larson, 1990); and H_2O (well-mixed at 0.176 ppm over the altitude range of interest, de Graauw et al., 1997).

3.2. Sources of Line data

The near-infrared spectral line database was updated from that used by Irwin et al. (1998); Roos-Serote et al. (1998) for Galileo/NIMS analysis, who predominantly used line data extracted from GEISA 1992 (Husson et al., 1992). HITRAN2004 (Rothman et al., 2005) was used for CO, H_2O, CH_4, CH_3D and $^{13}CH_4$. Absorption due to phosphine's pentad polyad dominates the VIMS 5-μm spectrum, with the $2\nu_2$ band at 5.07 μm and the broad $\nu_2 + \nu_4$ band between 4.69 and 4.78 μm. Furthermore, the ν_1 and ν_3 bands absorb shortward of 4.58 μm and contribute to the reduced thermal emission at these wavelengths. GEISA2003 (Jacquinet-Husson et al., 2005) was used for PH_3 as it contained updates from Kleiner et al. (2003) for some missing bands in the 5-μm window. However, the PH_3 absorption coefficients are still subject to considerable uncertainty, as the original intensity studies of Tarrago et al. (1992) are estimated to have only a 20-30% accuracy. Work is underway to compare this band to the dyad at 9 μm (Fusina and Di Lonardo, 2000; Brown et al., 2002) and the octad at 2.9 μm (Butler et al., 2006). GEISA2003 was also used for GeH_4, and contained updated 0-5300 cm^{-1} line data for NH_3 from Kleiner et al. (2003). AsH_3 was not present in either database, so we used line data from Dana et al. (1993) and Mandin (1995), following the NIMS analyses of Irwin et al. (1998); Roos-Serote et al. (1998).

Foreign broadening (by H_2) for each of the molecules was estimated for all lines as follows. GeH_4 was broadened with a half-width of 0.1 cm^{-1} atm^{-1} and a temperature dependence $T^{0.75}$ (Jacquinet-Husson et al., 2005). AsH_3 had a half width of 0.075 cm^{-1} atm^{-1} and $T^{0.5}$ (an assumption based on PH_3). PH_3 used es-

timated half-widths from Kleiner et al. (2003) and $T^{0.65}$. NH_3 had a half-width of 0.072 cm^{-1} atm^{-1} and $T^{0.73}$ (B. Bézard & L. Brown, *pers comms.*). The spectroscopic data for each gas were used to generate *k*-distributions (ranking absorption coefficients, *k*, according to their frequency distribution, Irwin et al., 2008) using a 16 nm FWHM on an evenly sampled wavelength grid of 8 nm spacing. We use a direct sorting method to calculate the *k*-distribution from line-by-line spectra within each spectral bin (e.g., Goody et al., 1989). A triangular instrument function was used for spectral modelling, which was found to be a good approximation for grating spectrometers with rectangular entrance slits and linear arrays of detectors, and allows rapid convolution over the *k*-distribution. The use of pre-tabulated *k*-distributions greatly accelerates spectral calculations and permits rapid retrieval of atmospheric spectra.

3.3. Forward Modelling and Retrieval

VIMS spectra were analysed using a suite of radiative transfer and retrieval codes developed at the University of Oxford (Nemesis, Irwin et al., 1997; Irwin et al., 2008), which have been previously used to investigate Galileo/NIMS near-IR spectra of Jupiter (e.g., Irwin et al., 1998; Irwin and Dyudina, 2002) and Cassini/CIRS thermal-IR spectra of Jupiter and Saturn (e.g., Fletcher et al., 2009a, 2010). The correlated-*k* method (Goody et al., 1989; Lacis and Oinas, 1991) is used for rapid calculation of non-monochromatic transmission along an inhomogeneous atmospheric path based upon pre-tabulated absorption coefficients, aerosol extinction cross-sections and collision-induced absorption. Retrievals of temperature, aerosol and gaseous composition are achieved using optimal estimation (Rodgers, 2000), but adapted for planetary applications by tuning *a priori* uncertainties to achieve the optimal trade-off between precision (the quality of the

spectral fit to the data) and physically-realistic solutions (Irwin et al., 2008). Retrievals require calculations of both the upwelling radiance, $I(\lambda)$, as well as the rate of change of radiance with the model parameters (dI/dx), based on the reference atmosphere (Section 3.1), which is perturbed in successive iterations (based on a Marquardt-Levenburg braking parameter, Press et al., 1992) to converge on the optimal solution. The algorithm seeks to minimise the residual between measured and modelled spectra (the traditional χ^2).

The 5-μm window can be modelled assuming thermal emission from the planet, attenuated by absorbing clouds. We neglect any thermal emission from the clouds themselves, as these reside at higher, cooler (by 50-80 K) altitudes than the source of the upwelling radiance (the 4-6 bar region, where temperatures reach approximately 240 K, see Section 3.5). In this case the functional derivatives (or Jacobians, dI/dx) are computed analytically, permitting rapid convergence to the optimal solution. However, multiple scattering from aerosols in the real Saturnian atmosphere will increase the optical paths of individual photons, thereby enhancing the gas absorptions and decreasing the molecular abundances required to reproduce the spectra.

The Nemesis software performs full multiple-scattering calculations (either for thermal emission, reflected sunlight or a combination of both) using a matrix operator (or doubling-adding) approach (Plass et al., 1973; Hansen and Travis, 1974) in a plane-parallel atmosphere, but numerical-differencing must be used to evaluate the functional derivatives due to the complexity of the multiple-scattering scheme. Integration of the scattered radiance over all solid angles was simplified in two ways: first, the integration over zenith angle used a Lobatto quadrature scheme with five angles to reduce the calculation to a simple weighted sum. The

scattering scheme must use sufficient zenith angle quadrature points to represent the phase functions of the scattering particles. Second, as thermal scattering is an azimuthally symmetric process, only the first (azimuthally-independent) Fourier component was used. The numerical calculations involved in multiple scattering are computationally expensive, slowing the retrieval process by an order of magnitude, but has a significant effect on the 5-μm window of the VIMS spectrum (Section 4).

3.4. Introducing Cloud Models

As knowledge of Saturn's vertical cloud structure and optical properties remains rather limited, we aimed to explore a broad range of parameter space with a variety of different cloud models (Table 3). A full vertical opacity retrieval was poorly constrained by the 5-μm data due to the degeneracy between PH_3 and aerosols. Instead, four parameterised vertical structure models were considered (optical depths are quoted for 5 μm);

- **I: Single Compact Cloud:** A single aerosol layer with variable optical thickness τ_1 and base pressure, p_b.
- **II: Two Compact Clouds:** A compact aerosol layer with a variable τ_1, composition and base pressure was placed beneath a spectrally-grey cloud at a fixed altitude with variable opacity, τ_2. This upper cloud was arbitrarily placed at the predicted NH_3 condensation altitude for a solar nitrogen abundance (1.47 bar, 152 K, Atreya et al., 1999) to minimise the number of free parameters in the model, although it would be deeper for bulk enrichments in Saturn's nitrogen content.

- **III: Single Extended Cloud:** A well-mixed distribution of aerosols with variable opacity τ_1 between the 100-mbar pressure level (the tropopause) and a variable base pressure, p_b.

- **IV: Compact Upper Cloud, Extended Deep Cloud:** A combination of the physically-thin upper cloud from Model II and the extended cloud from Model III.

In addition to the vertical structure, we tested the sensitivity to the aerosol composition by calculating extinction cross sections and phase functions $p(\theta)$ based on the refractive indices in Table 3 and shown graphically in Fig. 3. The models tested were (A) a grey cross-section and single scattering albedo (ω_0 = 0.95) across the 4.6-5.1 μm range, with an isotropic phase function (Fig. 4); (B) pure NH_3 ice (Martonchik et al., 1984); (C) pure NH_4SH (Ferraro et al., 1980); (D) a modified pseudo-NH_4SH cloud based on a refractive index of $2.3 + 0.01i$ (following suggestions by, Nixon et al., 2001); and (E) updated NH_4SH optical constants from Howett et al. (2007). For each cloud type in Table 3, Mie theory was used to calculate the scattering properties of spherical 1-μm-radius particles with a standard gamma distribution of particle sizes, variance 0.05 μm. The phase function $p(\theta)$ (shown in Fig. 4) was calculated as a two-term Henyey-Greenstein (HG) function (explicitly calculating the fraction of forward scattering and the asymmetries in the forward and backward scattering functions). With the exception of the isotropic scatterer, there is little to distinguish between the phase functions in Fig. 4, which are mostly determined by the chosen particle size. The crucial differences between the cloud models lies in the wavelength-dependence of the single scattering albedo (Fig. 3d, related to the imaginary refractive indices in Fig. 3a).

The absorption cross-sections, HG phase functions and size distributions in Figs. 3 and 4 were not intended to be an exhaustive representation of Saturn's clouds, given the substantial degeneracies inherent in the interpretation of VIMS spectra. Nevertheless, they are broadly representative of the types of condensed phases that might be present in Saturn's troposphere. Addition of further complexity (e.g., using the dual-absorber of NH_3 and NH_4SH following Sromovsky and Fry, 2010a, , or introduction of non-spherical particles) was not warranted by the 4.6-5.1 μm data, but such a combination is certainly possible for Saturn's cloud decks. Hydrazine (N_2H_4), from the photolysis of tropospheric NH_3, is not expected to be a major constituent of the tropospheric clouds, and the single scattering albedo and phase function in Figs. 3 and 4 (Clapp and Miller, 1996) are not sufficiently different in the 4.6-5.1 μm range to distinguish hydrazine from NH_3 ice in the VIMS spectrum. However, one important species is absent from Table 3 that could potentially be a major contributor to IR opacity in this spectral range - diphosphine (P_2H_4), which is expected to be present in significant quantities from PH_3 photolysis. Very little is known about the absorptive and scattering properties of P_2H_4, and a determination of the optical properties of diphosphene is an urgent priority for future VIMS studies, particularly in reflected sunlight. The uncertain spectral properties of non-spherical particles, NH_3+NH_4SH mixes, P_2H_4 and other potential contaminants in Saturn's clouds could significantly alter the retrieved opacities and cloud altitudes described in Section 5. Nevertheless, useful latitudinal contrasts in atmospheric parameters can still be derived.

3.5. Sensitivity Analysis

Synthetic spectra for each gas contributing to the 5-μm window are presented in Fig. 5. The mole fractions in the reference atmosphere were scaled by arbitrary

amounts to show their spectral influence (using a simple compact grey cloud, model II.A). PH_3, NH_3 and AsH_3 have the largest contributions to this range, with smaller influences from H_2O, GeH_4, CO and CH_3D. PH_3 in particular has a strong effect on the mean flux and spectral gradient between 4.9 and 5.0 μm. Variations of CH_4 and $^{13}CH_4$ have negligible effects on the spectra. Some of the spectral signatures are similar (e.g., AsH_3 and GeH_4, not to mention those of aerosol absorption and the broad effects of PH_3), leading to degeneracies in the interpretation of VIMS spectra, which will be explored below.

The vertical sensitivity of the spectra is highly dependent on the scattering properties and opacity of the cloud layers as well as the abundances of the absorbing gases. However, an estimate of the sensitivity is provided by the functional derivatives for the best-fitting II.A model (Fig. 6, using compact clouds at 1.4 and 2.7 bar and $\tau_1 = \tau_2 = 1$). The functional derivatives have been normalised, so that no account has been made for the magnitude of their spectral effects from Fig. 5. VIMS spectra are generally sensitive to abundance profiles in the 1-6 bar region, with peak sensitivity for PH_3, NH_3 and AsH_3 in the 1-3 bar range. Some gases (notably GeH_4, CO and CH_3D) show sensitivity to the 0.4-1.0 bar range, although these generally have a smaller overall effect on the spectrum. In the absence of absorbing cloud layers, contribution functions (Fig. 7, the product of the transmission weighting function, $d\tau/dz$, and the black body emission, $B(z,T)$) demonstrate that Saturn's thermal emission originates from the 4-6 bar region, where atmospheric temperatures reach approximately 240 K. In the absence of absorbing/scattering aerosols, the radiance in the 5-μm window would therefore be considerably larger than the 140-190 K brightness temperatures in Fig. 2.

4. Model Degeneracies and Validation

Modelling a single VIMS spectrum is relatively straightforward - a large number of gaseous and aerosol parameters can be tuned to provide an excellent fit to the low resolution VIMS spectra ($R \approx 330$ at 5 μm). However, the results must also be physically realistic when multiple retrievals are performed to study Saturn's zonal mean properties. Furthermore, the residuals between measured and synthetic spectra (the χ^2 parameter) should be as spatially uniform as possible to ensure that we have captured all of the variability in the model. This section will explore the degeneracies inherent in modelling VIMS nightside spectra in the absence of prior constraints on Saturn's aerosol optical properties and distributions. Through extensive tests of the model with different temperature, composition and cloud assumptions with the 22 coarse zonal-mean spectra described in Section 2.2, we demonstrate that VIMS data can provide robust conclusions about *relative* spatial variability, even if *absolute* abundances and opacities are poorly constrained.

4.1. Model Assumptions

We began by testing a number of assumptions in our forward models and retrievals. The simplest solution would be to fit the spectrum by varying $T(p)$ or PH_3 alone, in the absence of attenuating/scattering aerosols. However, thermal variations needed to be unrealistically large in the 1-5 bar region to reproduce the cool brightness temperatures observed in Fig. 2, and it proved impossible to reproduce the 4.6-4.9 μm and 4.9-5.1 μm regions simultaneously by varying PH_3 alone. Furthermore, fixing all the gases at their *a priori* distributions and varying the opacity of the simplest cloud model (I.A, a single compact grey-absorbing cloud in Table 3) failed to reproduce the spectrum. The VIMS spectra can only be reproduced by

a simultaneous retrieval of gaseous abundances and aerosol opacity.

But which gases to include in the retrieval? With the best-fitting aerosol distribution in the grey-absorbing case (both scattering and non-scattering), we sequentially added scaled retrievals of each gas (i.e., fixing the vertical profile but varying the absolute abundance) and assessed (a) the quantitative improvement to χ^2 and (b) the qualitative appearance of the meridional distribution from the 22 spectra. Variations of PH_3 were essential, whereas the importance of NH_3 only became apparent once we investigated equatorial latitudes where the spectrum near 5.1 μm appears markedly different from other regions (Fig. 2). The addition of AsH_3 moderately improved the fit in the region surrounding the broad absorption at 4.74 μm (this was especially true at low latitudes). However, although the remaining gases in the model (GeH_4, CO, H_2O and CH_3D) had some minor effects on the spectra, they did not deviate far from their *a priori* abundances and were deemed insignificant (using an F-statistic test, Bevington and Robinson, 1992). Omitting these four gases from the retrieval had negligible effects on the retrieved NH_3, PH_3 and AsH_3 abundances.

Adding complex cloud parameterisations: Simultaneously fitting for the spatial variation of PH_3, NH_3 and AsH_3, along with the variable opacity and depth of the single-cloud model I.A failed to provide adequate fits to the VIMS spectra. A similar conclusion was reached for Galileo/NIMS 5-μm spectra of Jupiter (e.g., Irwin et al., 2001), which required two separate aerosol populations, suggestive (but not uniquely) of a main jovian cloud deck of NH_4SH overlain by optically thin NH_3 clouds. This prompted the development of the 3 additional cloud models (II-IV) in Section 3.4 which immediately improved the fits to the VIMS spectra. The 2-cloud schemes produced the best fits as the two opacity sources were allowed

to vary independently of one another, increasing the number of free parameters available for the retrieval. In addition, experiments varying both the deep cloud base pressure (p_b) and opacity (τ_1) showed that they have sufficiently different spectral effects to make them separable. A comparison of the χ^2 values in Section 4.2 for the four different vertical models show that, while some can be ruled out, others gave such similar spectral results that they could not be distinguished from each other. Furthermore, the VIMS spectra are insensitive to location and extent of the upper cloud in models II and IV - shifting the base pressure between 1.4 and 1.8 bar for both compact and extended upper clouds had no effect on the fitted spectra, only the cumulative opacity (τ_2) has an influence.

Temperature variations in the deep troposphere: Independent retrievals of $T(p)$ from the 5-μm window would be impossible given the degeneracy with PH_3 and aerosols, although spatial variations are expected to be small. Nevertheless, three different assumptions were tested: (a) a mean CIRS-derived $T(p)$ from Cassini's prime mission (Fletcher et al., 2009a) with the same lapse rate g/c_p for all latitudes; (b) the same mean $T(p)$ but with a latitude-dependent lapse rate (i.e., varying with g); and (c) the full meridional CIRS $T(p)$ with a latitude-variable lapse rate. The last assumption provided the best fits to the VIMS spectra (there is VIMS sensitivity to $p < 800$ mbar in Figs. 6 and 7), although in practise there was little to differentiate between the three cases. Retrieved meridional distributions of NH_3 and AsH_3 were very similar for all three assumptions, but PH_3 and aerosol optical depths were affected. North-south asymmetries of PH_3 and aerosols were present for all three cases, but the PH_3 asymmetry was smaller when the CIRS-derived tropospheric temperature asymmetry was accounted for. Uncertainties in retrieved absolute values arising from the differing temperature

assumptions are 13%, 16% and 10% for PH_3, NH_3 and AsH_3, respectively; 33% and 50% for the deep and upper cloud opacities. Thus the retrieved gaseous composition and aerosols have a degeneracy with the deep atmospheric temperatures, but the best-fitting assumption (c) was used for the remainder of this study.

Vertical distribution of PH_3: Early models of VIMS spectra (e.g., Baines et al., 2009) assumed PH_3 to be well-mixed up to 0.55 bar (Fletcher et al., 2009a). However, it proved difficult to simultaneously fit the 4.6-4.7 μm radiances and the 4.8-5.0 μm spectral gradient. Fixing the PH_3 abundance at some mean for all latitudes generally worsened the quality of the spectral fits, particularly over the southern hemisphere (PH_3 was noted to be elevated in the southern troposphere, Fletcher et al., 2009a). Finally, we parameterised the vertical PH_3 distribution in terms of a deep mole fraction (q_0) up to a pressure level (p_0), followed by a decreasing abundance with altitude according to a fractional scale height, (f, the ratio of the gas scale height to that of the bulk atmosphere) (Fletcher et al., 2007a). Varying p_0 simultaneously with aerosols and other gaseous mole fractions for all 22 VIMS spectra (in both the scattering and non-scattering cases), we found optimum fits for p_0 between 1.1-1.3 bar (examples of the χ^2 surfaces for the equator, 30°N and 30°S are shown in Fig. 8). The cloud base and PH_3 p_0 were found to be at lower pressures (higher altitudes) at the equator than at mid-latitudes.

The introduction of the parameterised PH_3 profile had a substantial effect on the χ^2 at all latitudes, producing closer fits to both the 4.6-4.7 μm region and the spectral gradient between 4.8-5.0 μm. Similar tests for NH_3 and AsH_3 indicated that the well-mixed assumption was perfectly valid. However, the PH_3 p_0 determined by VIMS was considerably deeper than that determined by CIRS and sub-mm data (0.55-0.65 bar, Orton et al., 2000; Fletcher et al., 2009a). Further-

more, the retrieved fractional scale height was rather small, permitting negligible PH_3 abundances at $p < 1$ bar, again inconsistent with CIRS. Indeed, when we compared the range of PH_3 abundances derived from VIMS (3.0-5.5 ppm for the range of cloud models studied here, Section 5) to that derived from CIRS (5.4-8.2 ppm, with a mean of 6.4 ppm, Fletcher et al., 2009a), we found that VIMS and CIRS PH_3 abundances differed by factors of 1.5-1.8, even though the meridional variations of q_0 and f were similar from both instruments. Although CIRS is sensitive to lower pressures (300-800 mbar) than VIMS (2-3 bar), we expect PH_3 to be well-mixed between these two levels. It is unlikely that near-IR line strengths could be too strong by a factor of two, as this exceeds the uncertainties on line data for either the near-IR or mid-IR vibrational bands (Section 3.2). Identification of the source of this discrepancy will require (i) consistent measurements of PH_3 line data across multiple bands; (ii) higher spectral resolution observation of Saturn's emission to separate PH_3 absorption from continuum opacity sources; and (iii) simultaneous near and mid-IR retrievals in the presence of tropospheric aerosols. Nevertheless, *relative* PH_3 variations can still be derived from VIMS spectra.

4.2. Degeneracies in Spectral Modelling

At the start of this analysis, it was hoped that VIMS nightside spectra would constrain a unique cloud model and, independently, the spatial distribution of gases. However, the degeneracies between the different model parameters soon became overwhelming. Fig. 9 shows the meridional distribution of χ^2 for all four vertical models (I-IV), scattering and non-scattering cases, for optical models A-C (Figs. 3-4). Testing of models D (pseudo-NH_4SH cloud of Nixon et al., 2001) and E (updated NH_4SH optical constants by Howett et al., 2007) produced negligible differences to (i) the quality of the spectral fits and (ii) the meridional distributions

of gases and aerosols, so were omitted from the subsequent analysis. All cloud models produce poor fits poleward of 55°N due to a failure of our models to fit the higher emission angles (sensitive to higher altitudes in Saturn's atmosphere).

In general, the compact cloud models I and II produced the best fits to the spectra. The 2-cloud scheme fitted better at the equator (Fig. 9); at latitudes poleward of 10°S and the 35-65°N region of the northern hemisphere. However, the 2-cloud scheme cannot be distinguished from the single cloud scheme between 10-35°N, in a region where haze opacity is thought to be negligible (see Section 5). Finally, although the extended deep cloud models (III and IV) produced reasonable fits to the spectrum by eye, the χ^2 (Fig. 9) was sufficiently different to distinguish between the compact and extended cloud structures for the deep cloud.

In the non-scattering case, the residuals for optical models A-C (the grey, NH_3 and NH_4SH cloud compositions) were indistinguishable from one another. Modelling scattering within the clouds improved the fits for the grey isotropic scatterer and NH_4SH clouds, but not for NH_3 (although differences in the chosen particle sizes could have an effect on this conclusion). Ruling out pure NH_3 ice, the two remaining optical models produced very similar fits to the VIMS spectra: the grey assumption was better at northern mid-latitudes (10-40°N) whereas solid NH_4SH provided a better fit at all other latitudes (Fig. 9). Although this is certainly not a unique solution, the NH_4SH imaginary refractive indices in Fig. 3 from both Ferraro et al. (1980) and Howett et al. (2007) suggest smaller single scattering albedos between 4.7 and 4.9 μm compared to NH_3 ice or the other possible cloud compositions, even though the scattering phase functions (Fig. 4) are all very similar to one another. This difference provides marginally better fits for solid NH_4SH than other constituents, although we have not conducted an exhaustive

study of possible cloud candidates (e.g., the omission of diphosphine described in Section 3.4). In conclusion, the compact scattering cloud schemes (models I and II, with II doing better at known 'hazy' latitudes), in combination with the grey or NH_4SH optical properties (A and C) provided the best reproductions of the VIMS spectra.

4.2.1. Aerosol Profile Uncertainties

Given that no single cloud model provided the best fits to the data, we have to consider the range of possible solutions to this underconstrained problem. If compact cloud layers are used (models I-II), the base pressures for the opacity (p_b) must be placed between 1.9 and 2.7 bar. In the southern hemisphere, where the opacity of the upper cloud is highest, p_b is poorly constrained and can be at any pressure greater than 2 bar (see the χ^2 figures at the top of Fig. 12). Extended well-mixed clouds in the deep troposphere (models III-IV, previously shown to give poor reproductions of the VIMS data) require $p_b > 2.8$ bar, and typically place the bottom of the cloud between 3.3 and 4.0 bar.

The addition of scattering to the model causes the retrieved optical depths of the deep cloud (τ_1) and upper cloud (τ_2) to increase by factors of 2-5 relative to the non-scattering case (depending on the chosen optical model, Fig. 10). Furthermore, scattering introduces an emission-angle dependence to the deep optical depths if the cloud is an isotropic grey scatterer (Fig. 10a), but not when it is comprised of solid NH_4SH (Fig. 10b). As the emission angle is varying from equator to pole, this suggests that the isotropic phase function (Fig. 4) is a poor representation of Saturn's aerosols, as previous reflected sunlight studies of Saturn's clouds suggest a latitudinally-uniform τ_1 or an equator-to-pole decrease in opacity (e.g., Stam et al., 2001; Karkoschka and Tomasko, 2005). The NH_4SH scattering cloud

produced optical depths for the deep cloud which were largely independent of latitude (Fig. 10b). Ultimately the meridional variation of τ_1 cannot be uniquely determined unless (i) each latitude is viewed with the *same* emission angle; or (ii) multiple emission angles are used to separate the degenerate effects of emission angle and τ_1. No emission angle dependence is detected in retrievals of the upper cloud, τ_2 (Fig. 10c), which shows an asymmetry between northern and southern hemispheres for all of the cloud models tested (models II and IV featured the upper cloud), although the retrieved optical depths are highly dependent on the chosen aerosol model.

4.2.2. Degeneracies in Gaseous Composition

Unfortunately, the degeneracy between the different cloud models provides substantial uncertainties in the absolute abundances of gases derived from the 5-μm window. The *relative* variations of ammonia (shown in Fig. 11a for the grey-cloud optical model) are similar for all cloud models, but there are clear offsets in *absolute* abundance. The use of scattering clouds increases the pathlength for individual photons in the upper troposphere, and hence reduces the amount of each gas necessary to reproduce the absorption features (grey curves in Fig. 11 are systematically lower than the black non-scattering curves). Compact cloud models tend to yield smaller retrieved abundances than extended clouds, and even the best-fitting aerosol models differ in abundance by a factor of 2-3. Nevertheless, the enhanced NH_3 abundances at 45°N, 25°S and the equator are persistent features, irrespective of the chosen cloud model.

However, in the cases of AsH_3 and PH_3, the chosen cloud model can have a substantial effect on both the meridional structure and the absolute abundances. AsH_3 (Fig. 11b) shows a north-south asymmetry in the non-scattering case that

becomes much smaller when multiple scattering in the southern hemisphere is taken into account. The distribution of PH_3 is even more problematic, with a large scatter in measured abundances (Fig. 11c), although each aerosol model generally produces a north-south asymmetry in PH_3. The formal retrieval error on each PH_3 measurement is small, given that this gas dominates the shape of the VIMS spectrum, but the degeneracy between the cloud models makes a determination of the absolute abundance near-impossible without additional constraints.

The cause of this offset in absolute abundance is demonstrated in Fig. 12 for 15°N, 15°S and the equator (using non-scattering cloud model II.A), which shows how the algorithm converges to the optimal solution. There is a large variation of retrieved parameters with the cloud base pressure, showing how sensitive the absolute abundances are to the choice of aerosol model. As we described above, the deep cloud base pressure for the southern hemisphere (with the thickest upper cloud) is poorly constrained and could be placed anywhere at $p > 2$ bar (first row of Fig. 12). Placing cloud opacity at greater depth requires larger abundances of PH_3 (2nd row) and NH_3 (7th row), but smaller abundances of AsH_3 (6th row) to reproduce the absorption features. Furthermore, any variations in the deep cloud opacity τ_1 are largely compensated by the upper cloud τ_2 (4th and 5th rows of Fig. 12). This figure demonstrates the tradeoffs between the parameters in retrievals at each latitude, so we conclude that the *absolute* abundances and optical depths are dependent on the correct parameterisation of Saturn's clouds.

4.3. Validation Experiments

A robust way of demonstrating the validity of the retrieval scheme is to attempt extraction of the same variables from modelled VIMS spectra with simulated noise. 200 spectra were synthesised with non-scattering cloud model II.A

at a range of latitudes (±45°) and emission angles (0-45°); a range of *a priori* abundances for PH_3, NH_3, AsH_3 and GeH_4 (the latter as a control); and a range of values for the deep cloud τ_1 and p_b and upper cloud τ_2. The synthetic spectra were randomised using the same noise levels described for the real VIMS spectra (Section 2.1), and then the parameters were simultaneously retrieved from the synthetic spectra. Fig. 13 shows a positive correlation between the true values and retrieved values for each parameter, with the exception of GeH_4. The average deviations between modelled and retrieved values are: PH_3 (8%), AsH_3 (7.3%), NH_3 (30%), τ_1 (59%), τ_2 (25%) and p_b (17.6%). In addition, the NH_3 abundance appeared to be 30% lower than the true values, whereas the retrieved τ_1 was 54% larger than the input values. The large uncertainties on τ_1, τ_2 and p_b demonstrate the high correlation between these parameters, and the difficulties in separating them in the retrievals.

These simple experiments provide estimates of the uncertainties in absolute abundances based solely on random measurement errors. They do not represent the uncertainties due to systematic offsets. As we have seen, abundance uncertainties are dominated by the choice of cloud parameterisation rather than random error on the VIMS spectra. Relative spatial variability in retrieved quantities are more robust, and these will be presented in Section 5.

5. Results

Atmospheric composition (parameterised PH_3; well-mixed NH_3 and AsH_3) and aerosol properties (τ_1, τ_2 and p_b using the 2-cloud scheme, model II) were retrieved from 107 VIMS 4.6-5.1 μm spectra between 38°S and 67°N (planetocentric). The meridional distribution of each parameter is shown in Fig. 14, with

the zonal mean radiances and brightness temperatures at 5 μm indicated in the top panels and the best-fitting spectral models in Fig. 15. Given the difficulties in distinguishing between scattering and non-scattering cases with the grey or NH_4SH optical properties (models A and C) based on the χ^2 alone (Fig. 14b), we applied both techniques to the VIMS retrievals. Pure NH_3 ice and isotropic scattering were previously ruled out, although we stress that the retrieved atmospheric composition was very similar in these cases. The meridional distribution of χ^2 (Fig. 14b) shows a small improvement using multiple scattering with the phase function of NH_4SH, but the effect is insignificant within a $\Delta\chi^2 = 1$. Although the scattering cloud is more physically realistic, its inclusion has a substantial effect on retrieved parameters for such a small improvement in χ^2, so both sets of results are shown to highlight the degeneracy issue.

5.1. Saturn's Clouds

The retrieved properties of the compact cloud scheme are shown in Fig. 14c-e. The base pressure of the deep cloud is poorly constrained in the southern hemisphere where significant opacity due to aerosols in the upper cloud (Fig. 14c) and PH_3 (Figs. 14g-h) prevent a unique determination of the deep cloud base. The equatorial cloud is allowed to be present at lower pressures (approximately 2.1 bar) in the non-scattering case, compared to high pressures of the northern hemisphere cloud deck (2.5-2.8 bar). The need for this 2.1-bar equatorial cloud is removed when multiple scattering is used, when the equatorial cloud base becomes consistent with northern mid-latitudes. Both the scattering and non-scattering models agree on the cloud base pressures at northern mid-latitudes. Seasonally-variable cloud opacities in the 2-3 bar region are deemed unlikely given the long radiative timescales at these pressures, so a cloud base in the 2.5-2.8 bar region is

likely to exist globally on Saturn, with upward advection pushing the cloud higher at the equator.

Optical depths of the two clouds are higher in the multiple scattering case. The upper cloud τ_2 (arbitrarily placed at 1.4 bar, representative of the cumulative opacity of clouds and hazes above this pressure level) is more opaque in the southern hemisphere in both scattering and non-scattering cases. It is likely that the extended haze layers between the tropopause and 1.4 bar that are responsible for scattering of reflected sunlight on the dayside (Pérez-Hoyos et al., 2005) are also contributing to the attenuation of 5-μm flux on the nightside. Finally, the upper cloud shows enhanced equatorial opacity only in the multiple-scattering case. Increased equatorial opacity is qualitatively expected when we consider the 'hazy' appearance of Saturn's low latitudes in reflected sunlight (e.g., Porco et al., 2005; Vasavada et al., 2006) and the observations of vertical upwelling of the disequilibrium species PH_3 (Fletcher et al., 2009a).

The deep cloud opacity (Fig. 14d) shows opposing behaviours depending on the scattering assumptions. In the scattering case, we see a trend of increased opacity at high latitudes, whereas the opposite is true in the non-scattering case. A mean of the two would be uniform with latitude, which may be more realistic for the non-seasonal conditions in the 2-3 bar pressure regime. Small-scale variations in τ_1 of approximately 20-30% are colocated in the two cases, but the amplitude of the opacity variation is likely to depend on the spatial resolution of the VIMS images. Comparing to Fig. 1, the narrow axisymmetric bands of bright 5-μm flux are coincident with regions of lower opacity (particularly evident between 20-30°N). Fig. 14d suggests that these bright bands are regions of diminished opacity of the deep cloud layer, rather than being due to changes in the base pressure of the

2.5-2.8 bar cloud or the opacity of the upper 'haze'. Finally, unlike the elevated opacity of the upper cloud at low latitudes, there it nothing notable about the deep cloud opacity at the equator.

In summary, VIMS nightside spectra are consistent with clouds in two regimes - (i) a compact, meridionally-uniform cloud deck centred in the 2.5-2.8 bar region with small-scale opacity variations responsible for the narrow, bright axisymmetric lanes in VIMS images; and (ii) a hemispherically-asymmetric upper cloud above 1.4 bar, whose exact altitude and vertical structure are not constrained by VIMS, but which is likely to extend towards the tropopause and is responsible for reflected sunlight scattering. The upper cloud/haze is seasonally variable, whereas the deep cloud is not. Degeneracy between the scattering and non-scattering cases leads to uncertainties in absolute optical depths, and elevated equatorial opacity is only present in the scattering case.

Finally, although a 2.5-2.8 bar cloud deck of NH_4SH provided the best fits to the spectra for the limited range of clouds tested in this study, this solution is certainly non-unique and we cannot rule out a more complex combination of NH_3, NH_4SH and possibly P_2H_4 (see Section 3.4). The cloud deck is deeper than the predicted condensation altitudes for pure NH_3 (1.47-1.81 bar, Table 4 of Atreya et al., 1999, for solar and five-fold enrichments of heavy elements), but also higher than the predicted levels of NH_4SH (4.56-5.72 bar). Homogeneous cloud condensation occurs when the partial pressure of a gas exceeds its saturation vapour pressure. Formation of solid NH_4SH is more complex, involving a two-component reaction between NH_3 and H_2S whose equilibrium can be expressed by the empirical equation (Lewis, 1969; Atreya, 1986);

$$\log(p_{NH_3} p_{H_2S}) = 14.82 - \frac{4705}{T} \quad (1)$$

where p_{NH_3} and p_{H_2S} are the partial pressures of the two gases. Assuming that the abundances of the two gases are equal at the cloud condensation altitude (H_2S is completely used up in this reaction, whereas NH_3 survives to condense at higher, cooler altitudes), and comparing the saturated vapour pressure curve to Saturn's temperature profile, we require approximately 2 ppm of H_2S to form the VIMS 2.5-2.8 bar cloud. This would be produced by only 10% of the solar S/H ratio of Grevesse et al. (2007), considerably smaller than the 10× solar S/H abundance suggested by Briggs and Sackett (1989) (equivalent to 250 ppm), but larger than the 16 ppb upper limit of Weisstein and Serabyn (1996). Simple thermodynamic theory is a poor approximation to Saturn's true clouds, given that they are unlikely to be pure ice condensates and probably contain a range of impurities. The VIMS 2.5-2.8 bar cloud cannot be identified unambiguously using the present dataset.

5.2. Gaseous Composition

Figs. 14g-j show the meridional distributions of PH_3, NH_3 and AsH_3 in the scattering and non-scattering cases. In all three cases scattering increases the path length of individual photons and hence reduces the abundances required to reproduce the absorption features.

5.2.1. Phosphine

Section 4 demonstrated the uncertainties in the meridional distribution of phosphine under different scattering assumptions. The fractional scale height (representing the abundance for $p < 1.3$ bar) shows a local maximum at the equator under non-scattering conditions, consistent with the distribution identified by Cassini/CIRS in the 0.1-0.8 bar region (Fig. 7 of Fletcher et al., 2009a). Furthermore, VIMS successfully reproduces the mid-latitude asymmetry in the fractional

scale height, the local minimum at 10-20°S and the rising abundance towards 40°S observed by CIRS. The asymmetry in the fractional scale height at higher altitudes may be due to enhanced shielding by southern-hemisphere aerosols, increasing photolysis lifetimes in the south and allowing PH_3 to accumulate over the summer/autumn season.

But there are problems with these PH_3 results: (i) the knee pressure of the distribution (p_0 = 1.3 bar) is considerably deeper in the VIMS retrievals than the CIRS retrievals (p_0 = 0.55 bar); (ii) the deep mole fractions in the scattering (mean and standard error 3.1 ± 0.3 ppm) and non-scattering (4.4 ± 0.6 ppm) cases are smaller than the 6.4 ± 0.4 ppm mole fraction reported by CIRS (Fletcher et al., 2009a); (iii) both the scattering and non-scattering cases feature a local minimum in the deep ($p > 1.3$ bar) equatorial abundance which was not observed by CIRS (CIRS is insensitive to $p > 0.8$ bar); and (iv) the need for the equatorial enhancement in the fractional scale height is removed by the inclusion of scattering. Indeed, on the last point it seems that the PH_3 fractional scale height and the τ_2 of the upper cloud have exchanged roles in the retrievals, indicating a degeneracy between the two variables. The VIMS-derived mole fraction is also smaller than the disk-averaged 4.5-7.5 ppm range reported for Saturn's deep troposphere by Burgdorf et al. (2004), Lellouch et al. (2001), Orton et al. (2000), de Graauw et al. (1997) and Noll and Larson (1990). Finally, an asymmetry in the deep PH_3 abundance in the non-scattering case is deemed unlikely as the vertical mixing processes responsible for the presence of this disequlibrium species in the upper troposphere are not expected to be seasonally-variable. No deep asymmetries are observed in the multiple-scattering case.

Tests revealed that the use of the CIRS-derived mole fractions and p_0 could not

reproduce the VIMS spectrum adequately for any choice of cloud model, which leaves us with a conundrum - even though the meridional distributions are largely similar, the absolute values are quite different from the two instruments. As the same retrieval model was used in both studies, one possibility is that the line data for the pentad polyad at 5-μm are inconsistent with that of the dyad at 9 μm, making direct comparisons difficult. Indeed, the 5-μm line data are only accurate to the 20-30% level (Section 3.2), which may explain some of the discrepancy, but not all of it. Furthermore, just as VIMS retrievals are prone to PH_3 and aerosol degeneracies, CIRS retrievals are prone to $T(p)$-PH_3 degeneracies. Finally, the retrieved high-altitude PH_3 is determined by the absorption complex at 4.74-μm: if scattered light within the instrument artificially enhances the flux in this absorption band (see Section 2.1) then we would require less PH_3 than expected from CIRS. Further testing of the PH_3-aerosol degeneracy with improved knowledge of the cloud composition, along with consistent measurement of the PH_3 line data, is required to resolve this issue.

If we take the VIMS-derived PH_3 at face value, then some mechanism must be depleting PH_3 above the p_0 = 1.3-bar level. PH_3 is thought to be well-mixed by vertical diffusion at depth and depleted at higher altitudes due to photolysis to diphosphine (P_2H_4, a candidate for Saturn's haze) and elemental phosphorous. In the 1-3 bar region of VIMS sensitivity (Fig. 6), photochemical models suggest that production and loss rates are balanced due to recycling of P_2H_4 to PH_3 (J. Moses, *pers. comms.*), so depletion would be unexpected. If the PH_3 loss at $p < 1.3$ bar is real, then it may simply represent adjustment of the vertical profile between the well-mixed deep profile and the photolysis regime.

5.2.2. Ammonia

Unlike PH_3, the meridional distribution of NH_3 was similar for all of the aerosol models tested, even though the absolute abundances vary between scattering and non-scattering cases in Fig. 14i. Indeed, the largest discrepancy between scattering and non-scattering is at the equator and mid-southern latitudes, where the aerosol opacity was at its largest. NH_3 is enhanced at the equator between ±5° latitude by three times the northern mid-latitude abundances. This enhancement is coincident with the narrow region of diffuse brightness in Fig. 1, and with a narrow prograde jet identified by García-Melendo et al. (2010) which exists in addition to the broad equatorial jet. However, the NH_3 enhancement is confined to a much narrower equatorial region (±5°) than the CIRS-derived PH_3 enhancement (±20°) in the 0.2-0.8 bar region (Fletcher et al., 2009a).

Smaller enhancements are also notable in axisymmetric bands at 23-25°S and 42-47° (planetocentric), coinciding with dark lanes at 5.1 μm (Fig. 1). The northern hemisphere NH_3 peak exists between opposing zonal jets (prograde at 41°N, retrograde at 49°N), suggesting upwelling on the poleward side of the prograde jet. Interestingly, this jet was the location of a meandering lane known as the ribbon wave, first discovered by Voyager (e.g., Godfrey and Moore, 1986). The region north of the jet exhibited significant eddy activity associated with the wave (Godfrey and Moore, 1986), and appears to be the location of a dark band near 45°N flanked by 5-μm bright regions in Fig. 1. The northward gradient of potential vorticity (PV) was found to change sign at 44°N near to this jet, potentially violating the stability criterion of Arnol'd's second theorem (Read et al., 2009) and suggesting that the eddy activity (and possibly the enhanced NH_3 detected by VIMS) arises due to instabilities in the flow at depth. If the two hemispheres

are symmetric at depth, we might expect a similar NH_3 enhancement at southern mid-latitudes (44-51°S), and indeed Cassini imaging shows wave-like activity and an abundance of small vortices at this latitude (Vasavada et al., 2006; Choi et al., 2009). Unfortunately, these southern latitudes were not covered by the nightside VIMS spectra studied here.

The band at 23-25°S, which is embedded in the region of prograde flow associated with the equatorial jet, is also associated with a dark band in Fig. 1. The upwelling band is poleward of the warm South Equatorial Belt (SEB) at 14-17°S, and further north than Saturn's 'storm alley' (a region between 33-40°S characterised by an abundance of vortices, Vasavada et al., 2006), but may be associated with wave-like activity and tilted streaks observed in the same latitude band (Vasavada et al., 2006; Choi et al., 2009). Finally, despite these three regions of upwelling, we cannot unambiguously identify the sink regions of gaseous NH_3 required for continuity. However, depletion of gaseous NH_3 could be provided by (i) subsidence in regions flanking the upwelling, (ii) condensation to form fresh NH_3 clouds and (iii) photolysis to form hydrazine (a possible constituent of Saturn's tropospheric hazes).

Aside from these three regions of upwelling, the NH_3 abundance is reasonably uniform, varying between 120-180 ppm in the northern hemisphere, and slightly larger (120-220 ppm) in the south, depending on the scattering assumptions. Given the range of the results in Fig. 11, the NH_3 mole fraction derived from VIMS is uncertain by a factor of 2. For the best fitting cloud models we find globally-averaged abundances of 140 ± 50 ppm (scattering) and 200 ± 80 ppm (non-scattering) in the 1-4 bar sensitivity range of Fig. 6. The retrieved NH_3 abundance can be compared to the partial pressure for 100% relative humidity to

836 estimate the condensation altitudes for the gas. Equatorial NH_3 (500 ppm) would
837 condense near 1.65 bar, whereas the global mean abundance (140 ppm) suggests
838 condensation at 1.35 bar. This implies that NH_3 is saturated and well-mixed by
839 diffusive processes up to the 1.35-1.65 bar level (consistent with the expected
840 altitude of NH_3 condensation, Atreya et al., 1999), and then declines following
841 a saturated vapour-pressure curve and photolysis at lower pressures. Compared
842 to some of the previous disk-averaged NH_3 determinations in Table 1, we find
843 consistency with the 70-120 ppm values of Briggs and Sackett (1989), Grossman
844 et al. (1989), de Graauw et al. (1997, quoted for the 1.2-bar level), Orton et al.
845 (2000) and Burgdorf et al. (2004). The VIMS result is within the range of 50-200
846 ppm measured by Voyager/IRIS (Courtin et al., 1984) and slightly smaller than
847 the 500 ppm abundance at $p > 3$ bar derived from microwave spectra (de Pater
848 and Massie, 1985), except in the region of strong upwelling at the equator.

849 *5.2.3. Arsine*

850 AsH_3 is the principal arsenic-bearing gas on Jupiter and Saturn, though pre-
851 vious studies have focussed solely on globally-averaged values. The meridional
852 distribution of AsH_3 is shown in Fig. 14j for the first time. Both scattering and
853 non-scattering cases indicate local maxima flanking the equatorial region, centred
854 on 7°N and 7°S. The two maxima are much closer to the equator than the warm
855 tropospheric belts (±15°) observed by CIRS (Fletcher et al., 2007b). However, the
856 non-scattering case predicts an AsH_3 asymmetry (from around 4 ppb in the south
857 to 2.5-3.0 ppb in the north) that is not apparent in the scattering case (uniform
858 abundance of 2.2 ± 0.3 ppb in both hemispheres). The global mean abundances
859 of AsH_3 in the scattering (2.2 ± 0.3 ppb) and non-scattering (3.3 ± 0.8 ppb) cases
860 are consistent with ground-based measurements of 3.0 ± 1.0 ppb (Noll and Larson,

1990) and $2.4^{+1.4}_{-1.2}$ ppb (Bézard et al., 1989), although VIMS spectra do not have the spectral resolution to confirm the decreasing abundance with altitude (presumably due to photolysis) detected by Bézard et al. (1989).

Like PH_3, AsH_3 can be thought of as a tracer of tropospheric mixing, as its abundance at the altitudes studied by VIMS greatly exceeds thermochemical equilibrium predictions (e.g., Fegley and Lewis, 1979; Fegley and Lodders, 1994). This disequilibrium is thought to be caused by vertical transport, mixing parcels of air from the deep troposphere at a faster rate than AsH_3 can be chemically destroyed (conversion to solid phase As_4 or As_2S_2), thus the tropospheric AsH_3 abundance represents Saturn's equilibrium composition at much deeper levels (temperatures exceeding 400 K, Fegley and Lodders, 1994). Using the solar photospheric composition of Grevesse et al. (2007), we estimate a supersolar As/H ratio of 6.4-9.6 times solar (depending on the scattering and non-scattering assumptions), larger than the subsolar (0.6×) abundance on Jupiter (Noll et al., 1990), whereas P/H is supersolar on both planets (Fletcher et al., 2009a). As pointed out by Fegley and Lodders (1994), this difference is hard to explain because P and As exhibit similar cosmochemical behaviours, so we might expect equal enrichments of both elements during accretion.

6. Discussion: Possible Dynamical Mechanisms

While detailed dynamical modelling is deferred to future studies, here we discuss some plausible speculations concerning the dynamical processes responsible for the retrieved gaseous abundances and cloud distributions in Section 5. Fig. 14 indicated that the best-fitting VIMS models produce deep PH_3 ($p > 1.3$ bar) and AsH_3 distributions that do not show the same meridional variations as NH_3

and high-altitude PH_3 ($p < 1.3$ bar). In particular, deep PH_3 and AsH_3 showed local maxima either side of the equator, whereas the PH_3 scale height, the upper cloud opacity and NH_3 show maxima directly at the equator. At first glance this is difficult to interpret in terms of vertical transport from the deep troposphere, but the two different regimes may be reconciled if we consider a scenario where two stacked meridional circulation cells exist in Saturn's troposphere (see descriptions by, Del Genio et al., 2009; Ingersoll et al., 2000; Showman and de Pater, 2005).

Cloud-tracking observations of eddy-momentum convergence on both Jupiter and Saturn have long indicated that eddies accelerate the jets at pressures of 1 bar or deeper (Ingersoll et al., 1981; Salyk et al., 2006; Del Genio et al., 2007). In steady state, these eddy accelerations would be balanced by meridional flow that is equatorward across eastward jets and poleward across westward jets. This meridional flow also helped to explain the prevalence of thunderstorms in jovian belts (Gierasch et al., 2000; Ingersoll et al., 2000) and the distribution of NH_3 from radio observations (e.g., Fig. 3 of Showman and de Pater, 2005). However, these observations need to be reconciled with the 'classical' view of of the belt/zone circulation on giant planets, whereby air rises in low-temperature anticyclonic zones on the equatorial flanks of eastward jets and sinks in warmer cyclonic belts (e.g., Hess and Panofsky, 1951). The resulting meridional circulation causes poleward motion across eastward jets and equatorward motion across westward jets, opposing the flow suggested by the jet-pumping scenario described above. In steady state, the zonal Coriolis accelerations implied by this 'upper cell' circulation are balanced by an unidentified source of atmospheric 'drag' that decelerates the jets in the upper troposphere (Conrath and Pirraglia, 1983; Gierasch et al., 1986; Conrath et al., 1990).

The VIMS results require both the jet-pumping and the jet-damping circulation regimes to be invoked (the stacked-cell hypothesis). In this scenario, we suggest that drag within 20-30° of the equator enables a 'classical' meridional circulation in the upper cell. Air rises and diverges (cools) within the equatorial zone, advecting PH_3- and NH_3-rich air (along with aerosols to act as cloud nucleation sites) from depths below the NH_3 cloud into the upper troposphere to explain the equatorial maxima in Figs. 14c, g and i. This upper-cell air then moves poleward to 10-20°, where it descends and warms over the equatorial belts , leading to the relatively PH_3- and NH_3-depleted air at those latitudes. However, this classical upper-cell circulation must give way in the deeper troposphere to a circulation in the opposite sense. VIMS observations of off-equatorial maxima ($\approx \pm 10°$) in AsH_3 and deep PH_3 (Figs. 14h and j) suggest that air rises in the belts at 10-20°, moves equatorward and descends at the equator.

While we stress that the stacked-cell hypothesis may not be a unique explanation (and further predictive modelling is required), we note that these two different circulation regimes emerge quite naturally from considerations of momentum balance of the jets - the jet-pumping eddies on Jupiter and Saturn likely result from baroclinic instabilities or moist convection in the adiabatic region of the deep troposphere. However, convection and instabilities are largely inhibited in the stably-stratified upper troposphere so that eddies are confined to the deeper cell, leading to jet damping (and the opposite sense of meridional circulation) in the upper cell. The transition between the regimes of differing eddy behaviour (jet-pumping to jet-damping) may be set by the thermal stratification of the atmosphere, which grows larger in the upper troposphere. Numerical models of jet formation on the giant planets indeed show deep circulation cells whose tops close at 1 bar, al-

though they do not consistently capture the hypothesized upper cells and the jet decay with altitude, perhaps because the appropriate small-scale drag processes in the upper troposphere (e.g., absorption of small-scale gravity waves) are not represented (Lian and Showman, 2008). The mean circulation of the stacked cells would not be closed systems, as turbulent small-scale eddy transport would permit mixing of gases (e.g., mean flux of PH_3, NH_3 and AsH_3) and aerosols vertically between the cells, as well as creating temporal variability on the cell structure itself. Furthermore, the PH_3 and AsH_3 off-equatorial maxima have no counterparts in the zonal jet structure (which shows a broad prograde jet at the equator), but small-scale variations in the jet velocity (e.g., those recently detected by García-Melendo et al., 2010) may produce localised vorticity-mixing barriers that could be correlated with the distinct, narrow cloud lanes.

A second plausible explanation for the VIMS results involves eddy mixing, which could play an important role in transport of heat and gaseous species as they do on Earth (e.g., the Ferrel cell, where eddy heat transport dominates over mean transport). The mean circulation would produce cold equatorial temperatures on isobars in the upper cell (upwelling and divergence, as detected by Cassini/CIRS, Fletcher et al., 2007b) and warm temperatures in the deep cell (convergence and subsidence). A similar temperature pattern can also result from a single circulation cell in the presence of latent heating warming the atmosphere at depth (e.g., Fig. 9 of Lian and Showman, 2010). Because the air is statically stable, isentropes (surfaces of constant entropy) would bow upward at the equator in the upper cell and downward in the lower cell (e.g., Fig. 5 of Showman and Ingersoll, 1998). Mixing by eddy transport is almost isentropic on Saturn because of the long radiative time constant. Hence eddy mixing in the upper cell transports NH_3 and

PH_3-laden air upward and equatorward from greater pressures (off the equator) to lower pressures (at the equator). Similarly, eddy mixing in the deep cell would transport PH_3 and AsH_3-poor air downward and equatorward from lower pressures (off the equator) to greater pressures (at the equator). Thus quasi-isentropic mixing by eddies could occur simultaneously with a mean non-isentropic meridional flow (air crosses isentropes as it is heated and cooled), and both processes are capable of explaining the meridional distributions of PH_3, AsH_3 and NH_3 observed by VIMS.

Unfortunately, the spectral resolution of the VIMS data is too low to permit full 2D (i.e., latitude and altitude) retrievals of PH_3, AsH_3 and NH_3 which would allow further study of these different regimes. Furthermore, Section 4 indicated that the separation of gaseous composition and aerosol scattering/absorption is certainly non-unique. Although sensitivity extends over the 1-4 bar range in Fig. 6, we can obtain only a single 1D (i.e., latitudinal) estimate for AsH_3 and NH_3 abundances. Although the 1D distributions of these gases are consistent with the stacked-cell hypothesis, 2D distributions from high spectral-resolution mapping of these dynamical tracers is required to make advances in this field. However, this hypothesis may also explain why visible reflectivity (which exhibits albedo contrasts characteristic of the upper-cell meridional circulation in the jet-damping region) appears so different from Saturn's 5-μm appearance in Fig. 1 (representing the jet pumping in the deeper meridional cell).

7. Conclusions

Cassini/VIMS maps of Saturn's 4.6-5.1 μm nightside thermal emission have been used to study the latitudinal distribution of opacity sources in Saturn's tro-

posphere between 38°S and 67°N (planetocentric). The spatial variation of atmospheric composition (PH_3, NH_3 and AsH_3) and aerosol properties (the opacities of a compact 2.5-2.8 bar cloud and aerosols at $p < 1.4$ bar) are used to probe the vertical dynamics and chemistry in the NH_3 and NH_4SH ice cloud-forming regions of Saturn's troposphere. The spatial variability of Saturn's NH_3 and AsH_3 have been measured for the first time. Although the parameterisation of the aerosol model (scattering versus non-scattering; compact versus extended clouds; size distribution and refractive indices) has a significant effect on the retrieved opacities and gaseous abundances, we find that relative spatial variability can be retrieved reliably from the VIMS spectra even if absolute abundances remain uncertain. This study provides the following conclusions:

1. **VIMS Sensitivity:** Maps of Saturn's thermal emission at 4.6-5.1 μm reveal a previously unseen dynamical regime in the adiabatic region of the troposphere, with numerous narrow lanes of opacity variations (particularly the dark lane ±5° of the equator); a strong mid-latitude seasonal asymmetry in emission between ±5 – ±32°; and a plethora of discrete cloud features. This deep regime may be the region of eddy convergence which supplies momentum to the prograde jets (e.g., Del Genio et al., 2009), below the jet-drag region of the thermally-stratified upper troposphere. However, VIMS spectra are also sensitive to upper tropospheric clouds/hazes, with a seasonally-generated asymmetry in opacity attenuating the thermal emission. Extensive testing of the retrieval model indicated VIMS sensitivity to both atmospheric composition (parameterised PH_3, well-mixed NH_3 and AsH_3, but not GeH_4, CO, H_2O or CH_4) and cloud properties.
2. **Saturn's Clouds:** Spectral fitting was consistent with cloud opacity in two

regimes - (i) a compact, meridionally-uniform cloud deck centred in the 2.5-2.8 bar region with small-scale opacity variations (20-30% at the resolution of the VIMS images used in this study) responsible for the narrow, bright axisymmetric lanes in VIMS images; and (ii) a hemispherically asymmetric upper cloud above the 1.4-bar level, whose exact altitude and vertical structure are not constrained by VIMS, but which is likely to extend towards the tropopause and is responsible for reflected sunlight scattering on the dayside. The upper cloud shows a 1.5-2.0 times enhanced opacity within ±10° of the equator. A scheme with a single-cloud layer was indistinguishable from the 2-cloud scheme at northern mid-latitudes, where the opacity of the upper cloud is at its smallest. The deep cloud base is poorly constrained in the southern hemisphere (it must exist at $p > 2$ bar) where the opacity of the upper cloud is at its largest. The meridional opacity distribution is highly sensitive to the optical properties of the clouds, but of the limited range of cloud compositions tested here, the optical constants of NH_4SH provided the best fits to the VIMS spectra. The deep cloud is not likely to consist of pure NH_3 ice, but more complex cloud compositions (e.g., a mixture of NH_3 and NH_4SH; or the presence of P_2H_4 and other contaminants) cannot be ruled out. The 2.5-2.8 bar cloud is deeper than the predicted condensation altitude of NH_3 (1.81 bar for a 5× enrichment of heavy elements, Atreya et al., 1999) and higher than the predicted levels for NH_4SH condensation (5.72 bar), so its composition cannot be identified unambiguously.

3. **Phosphine:** PH_3 dominates the morphology of the 5-μm spectrum, but its meridional variation is highly sensitive to the choice of cloud model. A well-mixed PH_3 distribution failed to reproduce the spectrum, and we found

that the abundance begins to decline for $p < 1.3$ bar (lower pressures at the equator). The fractional scale height for the upper-tropospheric PH_3 generally showed a maximum at the equator and a mid-latitude asymmetry (consistent with the results from Cassini/CIRS, Fletcher et al., 2009a). The deep PH_3 showed an equatorial minimum flanked by two off-equatorial maxima (±10°). However, deep mole fractions in the scattering (mean and standard error 3.1 ± 0.3 ppm) and non-scattering (4.4 ± 0.6 ppm) cases were smaller than the 6.4 ± 0.4 ppm mole fraction reported by CIRS, and the $p_0 = 1.3$-bar transition from the well-mixed to the photolysis region was much deeper than that derived from CIRS ($p_0 = 0.55$ bar). Uncertainties in the cloud spectral properties, as well as the PH_3 line data, are the likely source of this CIRS-VIMS discrepancy, requiring joint modelling to resolve this issue.

4. **Ammonia:** NH_3 has a significant effect on the spectrum near 5.1 μm and a similar spatial distribution for all cloud models tested, being elevated within ±5° of the equator (in a region of strong 5-μm attenuation) by three times the northern mid-latitude abundances. Extratropical upwelling is also suggested by small enhancements at 23-25°S and 42-47°N. The northern peak is associated with a 5-μm dark band just north of the prograde jet at 41°N, and may be associated with abundant eddy activity and the 'ribbon wave' at this latitude. Aside from the three regions of upwelling, the NH_3 abundance was latitudinally uniform, with globally averaged 1-3 bar abundances of 140 ± 50 ppm (scattering) and 200 ± 80 ppm (non-scattering), rising to 300-500 ppm at the equator.
5. **Arsine:** The spatial variability of Saturn's principal arsenic-bearing gas has

been measured for the first time, showing local maxima at ±7° and a minimum at the equator. An AsH_3 asymmetry (from around 4 ppb in the south to 2.5-3.0 ppb in the north) was detected using non-scattering clouds, but is not apparent in the more physically-realistic scattering models (uniform abundance of 2.2 ± 0.3 ppb in both hemispheres). This results in a supersolar As/H ratio of 6.4-9.6 times solar, larger than the subsolar (0.6×) abundance on Jupiter. This difference between the two gas giants is unexpected, as P/H is supersolar on both planets and the two species should have shared many common properties during planetary accretion.

Exploitation of the 5-μm window by Cassini/VIMS has revealed a planet with symmetric dynamics at depth coupled to substantial seasonal asymmetries in the upper troposphere. However, uncertainties in the properties and distribution of Saturn's clouds produces significant degeneracies in modelling the VIMS data. Future work should focus on (a) comparing dayside 4.6-5.1 μm spectra to those on the nightside to quantify the effects of sunlight scattering; (b) exploiting 1-4 μm reflection spectroscopy of Saturn's clouds to constrain the vertical aerosol distribution and phase function; (c) incorporating new constraints on aerosol size distributions and optical properties to constrain gaseous retrievals; and (d) producing regional maps of isolated dynamic features to qualitatively assess the physical reality of the retrieval model. Future near-infrared instruments for giant planet exploration should feature improved spectral resolutions in the 5-μm window to break the degeneracies between aerosols and composition and permit fully 3-dimensional retrievals to trace tropospheric dynamics within and beneath the condensation clouds.

Acknowledgments

Fletcher was supported during this research by a Glasstone Science Fellowship at the University of Oxford. Irwin acknowledges the support of the UK Science and Technology Facilities Council. Orton carried out part of this research at the Jet Propulsion Laboratory, California Institute of Technology, under a contract with NASA, and acknowledges support from the Cassini Project. We thank the members of the VIMS investigation team who have assisted in the design of the imaging sequences, instrument commands and other vital operational tasks, and the Ground Systems Operations for the Cassini Project. This research has made use of the USGS Integrated Software for Imagers and Spectrometers (ISIS).

Figure Captions

Figure 1: Four examples of the VIMS-IR radiances at (a) 5.1; (b) 5.0; (c) 4.8 and (d) 4.6 μm. Radiances from eight cubes in Table 2 were reprojected onto a cylindrical map, selecting only regions that were well separated from the day/night terminator. No attempt has been made to correct for the motion of cloud features due to the zonal flow (see main text), resulting in some apparent disconnect at the overlap points. We have not corrected for limb darkening in these images, resulting in the visible seams where the cubes overlap. Thermal emission was obscured by the noise at wavelengths shorter than 4.5 μm.

Figure 2: Comparisons of zonally-averaged radiances (a) and brightness temperatures (b) for five latitudes (the equator, $\pm$15 and $\pm$30°) extracted from the image cubes in Fig. 1. Prominent features in the spectrum are labelled in panel (b) in their approximate locations, but these gases actually have effects over a wider region of the low-resolution VIMS spectrum than indicated here. Radiance errors described in the main text are indicated in panel (a).

Figure 3: Optical constants for the range of cloud compositions considered in this study (a key for the different lines is shown in (b). Imaginary (a) and real (b) refractive indices are taken from the listed references. Extinction cross-sections (c) and single scattering albedoes (d) were calculated using Mie theory for a standard gamma distribution of particles of radius $r = 1.0 \pm 0.05$ μm. The key difference between the compositions is the enhanced absorption of NH_4SH-like species (Ferraro et al., 1980; Howett et al., 2007) between 4.7 and 4.9 μm.

Figure 4: Variation of phase function with scattering angle for the range of cloud compositions used in this study. Phase functions were calculated as a two-term Henyey-Greenstein (HG) functions based on the optical properties listed in

the key. With the exception of the isotropic scatterer, there is little to distinguish between these phase functions, which is mostly governed by the choice of particle sizes ($r = 1.0 \pm 0.05$ μm).

Figure 5: Sensitivity of VIMS nightside spectra to a selection of gases in the model atmosphere. Spectra were calculated using a compact grey-absorbing cloud in the absence of scattering, with molecular abundances scaled from 0.1-10 times the *a priori* values (key is shown in panel i). PH_3, NH_3 and AsH_3 have the largest effects over this spectral range.

Figure 6: Examples of the functional derivatives (Jacobians, the rate of change of radiance with a particular model parameter) for temperature and several gases contributing to the 5-μm window. Spectra were calculated using a compact grey-absorbing cloud (model II.A), so results will vary depending on the properties of the absorbing gases. Jacobians have been normalised to unity for each gas, and this does not represent their relative contribution to the spectrum (see Fig. 5, for example). A scale bar is shown for the central three panels. VIMS spectra are mostly sensitive to compositional variations in the 1-3 bar region.

Figure 7: Contribution function (product of the transmission weighting function and the Planck black body function) calculated for a cloud-free case for the VIMS spectrum. The contribution function shows a maximum sensitivity to the 5-bar level.

Figure 8: Contours of χ^2 for VIMS retrievals varying the base pressure p_b of the deep cloud layer and the transitional pressure p_0 from well-mixed deep PH_3 to PH_3 in the photochemical depletion region. Three representative latitudes are shown, indicating that the best fitting p_0 is 1.3 bar, although this can be at lower pressures at the equator.

Figure 9: The meridional distribution of χ^2 for optical models A-C (grey, NH_3 and NH_4SH cloud scattering properties), which depend on the scattering processes (T=non-scattering, S=scattering) and vertical models (I-IV). These retrievals were performed for 22 coarsely gridded VIMS zonal mean spectra using the grey-cloud approximation. Comparison of these values was used to rule out certain optical models and vertical distributions, although considerable degeneracies still exist.

Figure 10: Demonstration of the dependence of retrieved cloud optical depths on the chosen aerosol models (T=non-scattering, S=scattering). Panels (a) and (b) show the opacity of the deep cloud and the spurious emission angle dependence when grey scatterers are assumed. Panel (c) shows that the north-south asymmetry in upper-cloud opacity is present for all model assumptions. The corresponding χ^2 are shown in Fig. 9.

Figure 11: Demonstration of the degeneracy in gaseous distributions of NH_3, AsH_3 and PH_3 depending on the choice of aerosol optical models (T=non-scattering, S=scattering) and vertical models (I-IV). The corresponding χ^2 are shown in Fig. 9.

Figure 12: Trade off between the different atmospheric parameters for three latitudes, 15°S (left column), the equator (central column) and 15°N (right column). The seven rows show (a) the variation of χ^2/N with base pressure, where N is the number of spectral channels ($N = 32$, so a $\Delta\chi^2 = 1$ envelope corresponds to 0.03 in these panels) in the retrieval; (b-c) the PH_3 deep mole fraction and fractional scale height; (d-e) the opacity of the deep and upper clouds in model II.A; (f-g) the well-mixed mole fractions of AsH_3 and NH_3. The vertical dashed line shows the best-fitting base pressure for each latitude (note that it is poorly

constrained in the southern hemisphere case).

Figure 13: Scatter plots showing positive correlations between synthetic VIMS spectral inputs ('true' values) and the retrieved outputs. The only figures showing no correlation is GeH_4, which cannot be reliably retrieved from the VIMS data. The deviation between true and retrieved parameters (the dotted line shows a 1:1 relationship) is used to define the random error on retrieved quantities.

Figure 14: Meridional distributions of Saturn's cloud and aerosol properties (panels c-e) and gaseous distributions (panels g-j), for the two best-fitting cloud models: an upper haze and a deep compact cloud, with the non-scattering grey assumption (solid line, model A) and the scattering NH_4SH assumption (dotted line, model C). These are compared to the zonal mean radiances and brightness temperatures in panels a and f, respectively. Although the scattering model shows a small improvement in χ^2 in panel a, suggesting that the optical properties of NH_4SH produce the best results, this improvement is deemed insignificant given the degeneracies discussed in the main text. The points with error bars at 60°S show the formal retrieval uncertainty in each quantity.

Figure 15: The best-fitting spectral models to five selected latitudes. Both the thermal non-scattering and NH_4SH scattering models (lines) produce near-identical fits to the data (individual points). Overfitting at 4.67 and 4.85 μm, and underfitting at 5.06 μm, are common features of all spectral models and could not be explained by the addition of further gaseous species.

References

Atreya, S. K., 1986. Atmospheres and Ionospheres of the Outer Planets and their Satellites. Vol. 15 of Physics and Chemistry in Space. Springer-Verlag Berlin

Heidelberg.

Atreya, S. K., Wong, M. H., Owen, T. C., Mahaffy, P. R., Niemann, H. B., de Pater, I., Drossart, P., Encrenaz, T., 1999. A comparison of the atmospheres of Jupiter and Saturn: deep atmospheric composition, cloud structure, vertical mixing, and origin. Plan. & Space Sci. 47, 1243–1262.

Baines, K. H., Drossart, P., Momary, T. W., Formisano, V., Griffith, C., Bellucci, G., Bibring, J. P., Brown, R. H., Buratti, B. J., Capaccioni, F., Cerroni, P., Clark, R. N., Coradini, A., Combes, M., Cruikshank, D. P., Jaumann, R., Langevin, Y., Matson, D. L., Mccord, T. B., Mennella, V., Nelson, R. M., Nicholson, P. D., Sicardy, B., Sotin, C., 2006. The Atmospheres of Saturn and Titan in the Near-Infrared: First Results of Cassini/VIMS. Earth, Moon, and Planets , 1–29.

Baines, K. H., Momary, T. W., Fletcher, L. N., Showman, A. P., Roos-Serote, M., Brown, R. H., Buratti, B. J., Clark, R. N., Nicholson, P. D., Dec. 2009. Saturn's north polar cyclone and hexagon at depth revealed by Cassini/VIMS. Plan. & Space Sci. 57, 1671–1681.

Baines, K. H., Momary, T. W., Roos-Serote, M., the Cassini/VIMS Science Team, 2006. North vs South on Saturn: Discovery of a Pronounced Hemispherical Asymmetry in Saturn's 5-Micron Emission and Associated Deep Cloud Structure by Cassini/VIMS. B.A.A.S. 38, 488.

Bevington, P. R., Robinson, D. K., 1992. Data reduction and error analysis for the physical sciences, 2nd Edition. WBC/McGraw-Hill, New York.

Bezard, B., Baluteau, J. P., Marten, A., Jun. 1983. Study of the deep cloud struc-

ture in the equatorial region of Jupiter from Voyager infrared and visible data. Icarus 54, 434–455.

Bézard, B., Drossart, P., Lellouch, E., Tarrago, G., Maillard, J. P., 1989. Detection of arsine in Saturn. Astrophys. J. 346, 509–513.

Borysow, A., 1991. Modelling of collision-induced infrared-absorption spectra of H_2-H_2 pairs in the fundamental band at temperatures from 20K to 300K. Icarus 92, 273–279.

Borysow, A., 1993. Modelling of collision-induced infrared-absorption spectra of H_2-H_2 pairs in the fundamental band at temperatures from 20 to 300K. Icarus 106, 614.

Borysow, A., Frommhold, L., 1986. Theoretical collision-induced rototranslational absorption spectra for the outer planets: H_2-CH_4 pairs. Astrophys. J. 304, 849–865.

Borysow, A., Frommhold, L., 1987. Collision-induced rototranslational absorption spectra of CH_4-CH_4 pairs at temperatures from 50 to 300K. Astrophys. J. 318, 940–943.

Borysow, J., Frommhold, L., Birnbaum, G., 1988. Collison-induced rototranslational absorption spectra of H_2-He pairs at temperatures from 40 to 3000 K. Astrophys. J. 326, 509–515.

Briggs, F. H., Sackett, P. D., 1989. Radio observations of Saturn as a probe of its atmosphere and cloud structure. Icarus 80, 77–103.

1235 Brown, L., Sams, R., Kleiner, I., Cottaz, C., Sagui, L., 2002. Line intensities of the
1236 phosphine dyad at 10 μm. Journal of Molecular Spectroscopy 215 (2), 178–203.

1237 Brown, R. H., Baines, K. H., Bellucci, G., Bibring, J., Buratti, B. J., Capac-
1238 cioni, F., Cerroni, P., Clark, R. N., Coradini, A., Cruikshank, D. P., Drossart,
1239 P., Formisano, V., Jaumann, R., Langevin, Y., Matson, D. L., McCord, T. B.,
1240 Mennella, V., Miller, E., Nelson, R. M., Nicholson, P. D., Sicardy, B., Sotin,
1241 C., Dec. 2004. The Cassini Visual And Infrared Mapping Spectrometer (Vims)
1242 Investigation. Space Science Reviews 115, 111–168.

1243 Burgdorf, M. J., Orton, G. S., Encrenaz, T., Davis, G. R., Lellouch, E., Sidher,
1244 S. D., Swinyard, B. M., 2004. Far-infrared spectroscopy of the giant planets:
1245 measurements of ammonia and phosphine at Jupiter and Saturn and the contin-
1246 uum of Neptune. Advances in Space Research 34, 2247–2250.

1247 Butler, R., Sagui, L., Kleiner, I., Brown, L., 2006. The absorption spectrum of
1248 phosphine (ph3) between 2.8 and 3.7 μm: Line positions, intensities, and as-
1249 signments. Journal of Molecular Spectroscopy 238 (2), 178–192.

1250 Choi, D. S., Showman, A. P., Brown, R. H., Apr. 2009. Cloud features and zonal
1251 wind measurements of Saturn's atmosphere as observed by Cassini/VIMS.
1252 Journal of Geophysical Research (Planets) 114, 4007.

1253 Clapp, M. L., Miller, R. E., Oct. 1996. Complex Refractive Indices of Crystalline
1254 Hydrazine from Aerosol Extinction Spectra. Icarus 123, 396–403.

1255 Conrath, B. J., Gautier, D., 2000. Saturn Helium Abundance: A Reanalysis of
1256 Voyager Measurements. Icarus 144, 124–134.

Conrath, B. J., Gierasch, P. J., Leroy, S. S., 1990. Temperature and circulation in the stratosphere of the outer planets. Icarus 83, 255–281.

Conrath, B. J., Pirraglia, J. A., 1983. Thermal structure of Saturn from Voyager infrared measurements - Implications for atmospheric dynamics. Icarus 53, 286–292.

Courtin, R., Gautier, D., Marten, A., Bézard, B., Hanel, R., 1984. The composition of Saturn's atmosphere at northern temperate latitudes from Voyager IRIS spectra - NH_3, PH_3, C_2H_2, C_2H_6, CH_3D, CH_4, and the Saturnian D/H isotopic ratio. Astrophys. J. 287, 899–916.

Cuzzi, J. N., Clark, R. N., Filacchione, G., French, R., Johnson, R., Marouf, E. A., Spilker, L. J., 2009. Ring Particle Composition and Size Distribution, In: Saturn from Cassini-Huygens. Springer, Ch. 15, pp. 459–509.

Dana, V., Mandin, J.-Y., Tarrago, G., W.B., O., Drossart, P., 1993. Absolute infrared intensities in the fundamentals ν_1 and ν_3 of arsine. Journal of molecular spectroscopy 159 (22), 468–480.

de Graauw, T., Feuchtgruber, H., Bézard, B., Drossart, P., Encrenaz, T., Beintema, D. A., Griffin, M., Heras, A., Kessler, M., Leech, K., Lellouch, E., Morris, P., Roelfsema, P. R., Roos-Serote, M., Salama, A., Vandenbussche, B., Valentijn, E. A., Davis, G. R., Naylor, D. A., 1997. First results of ISO-SWS observations of Saturn: detection of CO_2, CH_3C_2H, C_4H_2 and tropospheric H_2O. Astron. Astrophys. 321, L13–L16.

de Pater, I., Massie, S. T., 1985. Models of the millimeter-centimeter spectra of the giant planets. Icarus 62, 143–171.

Del Genio, A. D., Achterberg, R. K., Baines, K. H., Flasar, F. M., Read, P. L., Sánchez-Lavega, A., Showman, A. P., 2009. Saturn Atmospheric Structure and Dynamics, In: Saturn from Cassini-Huygens. Springer, Ch. 6, pp. 113–159.

Del Genio, A. D., Barbara, J. M., Ferrier, J., Ingersoll, A. P., West, R. A., Vasavada, A. R., Spitale, J., Porco, C. C., 2007. Saturn eddy momentum fluxes and convection: First estimates from Cassini images. Icarus 189, 479–492.

Fegley, B., Lewis, J. S., May 1979. Thermodynamics of selected trace elements in the Jovian atmosphere. Icarus 38, 166–179.

Fegley, B. J., Lodders, K., 1994. Chemical models of the deep atmospheres of Jupiter and Saturn. Icarus 110, 117–154.

Ferraro, J. R., Sill, G., Fink, U., Sep. 1980. Infrared Intensity Measurements of Cryodeposited Thin Films of NH_3, NH_4HS, H_2S, and Assignments of Absorption Bands. Applied Spectroscopy 34, 525–533.

Fink, U., Larson, H. P., Jul. 1978. Deuterated methane observed on Saturn. Science 201, 343–345.

Fink, U., Larson, H. P., Bjoraker, G. L., Johnson, J. R., May 1983. The NH3 spectrum in Saturn's 5 micron window. ApJ 268, 880–888.

Fletcher, L. N., Achterberg, R. K., Greathouse, T. K., Orton, G. S., Conrath, B. J., Simon-Miller, A. A., Teanby, N., Guerlet, S., Irwin, P. G. J., Flasar, F. M., Jul. 2010. Seasonal change on Saturn from Cassini/CIRS observations, 2004-2009. Icarus 208, 337–352.

Fletcher, L. N., Irwin, P. G. J., Teanby, N. A., Orton, G. S., Parrish, P. D., Calcutt, S. B., Bowles, N., de Kok, R., Howett, C., Taylor, F. W., May 2007a. The meridional phosphine distribution in Saturn's upper troposphere from Cassini/CIRS observations. Icarus 188, 72–88.

Fletcher, L. N., Irwin, P. G. J., Teanby, N. A., Orton, G. S., Parrish, P. D., Calcutt, S. B., de Kok, R., Howett, C., Bowles, N., Taylor, F. W., 2007b. Characterising Saturn's Vertical Temperature Structure from Cassini/CIRS. Icarus 189, 457–478.

Fletcher, L. N., Orton, G. S., Teanby, N. A., Irwin, P. G. J., Aug. 2009a. Phosphine on Jupiter and Saturn from Cassini/CIRS. Icarus 202, 543–564.

Fletcher, L. N., Orton, G. S., Teanby, N. A., Irwin, P. G. J., Bjoraker, G. L., Feb. 2009b. Methane and its isotopologues on Saturn from Cassini/CIRS observations. Icarus 199, 351–367.

Fusina, L., Di Lonardo, G., 2000. The $\nu 2$ and $\nu 4$ bending fundamentals of phosphine (ph3). Journal of Molecular Structure 517, 67–78.

Gaddis, L., Anderson, J., Becker, K., Becker, T., Cook, D., Edwards, K., Eliason, E., Hare, T., Kieffer, H., Lee, E. M., Mathews, J., Soderblom, L., Sucharski, T., Torson, J., McEwen, A., Robinson, M., Mar. 1997. An Overview of the Integrated Software for Imaging Spectrometers (ISIS). In: Lunar and Planetary Institute Science Conference Abstracts. Vol. 28 of Lunar and Planetary Institute Science Conference Abstracts. pp. 387–+.

García-Melendo, E., Sánchez-Lavega, A., Legarreta, J., Perez-Hoyos, S., Hueso,

1323 R., Nov. 2010. A strong high altitude narrow jet detected at Saturn's equator.
1324 Geophys. Res. Lett. 37, L22204.

1325 Gierasch, P. J., Ingersoll, A. P., Banfield, D., Ewald, S. P., Helfenstein, P., Simon-
1326 Miller, A., Vasavada, A., Breneman, H. H., Senske, D. A., Galileo Imaging
1327 Team, Feb. 2000. Observation of moist convection in Jupiter's atmosphere. Na-
1328 ture 403, 628–630.

1329 Gierasch, P. J., Magalhaes, J. A., Conrath, B. J., Sep. 1986. Zonal mean properties
1330 of Jupiter's upper troposphere from Voyager infrared observations. Icarus 67,
1331 456–483.

1332 Godfrey, D. A., Moore, V., 1986. The Saturnian ribbon feature - A baroclinically
1333 unstable model. Icarus 68, 313–343.

1334 Goody, R., West, R., Chen, L., Crisp, D., Dec. 1989. The correlated-k method for
1335 radiation calculations in nonhomogeneous atmospheres. Journal of Quantitative
1336 Spectroscopy and Radiative Transfer 42, 539–550.

1337 Grevesse, N., Asplund, M., Sauval, A., 2007. The Solar Chemical Composition.
1338 Space Science Reviews 130 (1), 105–114.

1339 Grossman, A. W., Muhleman, D. O., Berge, G. L., 1989. High-resolution mi-
1340 crowave images of Saturn. Science 245, 1211–1215.

1341 Hansen, J. E., Travis, L. D., 1974. Light scattering in planetary atmospheres.
1342 Space Science Reviews 16, 527–610.

1343 Hess, S. L., Panofsky, H. A., 1951. The Atmospheres of the Other Planets. Vol.

1344 Compendium of Meteorology. American Meteorological Society, Boston, pp.
1345 391–398.

1346 Howett, C. J. A., Carlson, R. W., Irwin, P. G. J., Calcutt, S. B., Jan. 2007. Opti-
1347 cal constants of ammonium hydrosulfide ice and ammonia ice. Journal of the
1348 Optical Society of America B Optical Physics 24, 126–136.

1349 Husson, N., Bonnet, B., Scott, N., Chedin, A., 1992. Management and Study of
1350 Spectroscopic Information-The GEISA program. Journal of Quantitative Spec-
1351 troscopy and Radiative Transfer 48, 509–518.

1352 Ingersoll, A., Beebe, R., Mitchell, J., Garneau, G., Yagi, G., Muller, J., 1981.
1353 Interaction of eddies and mean zonal flow on Jupiter as inferred from Voyager
1354 1 and 2 images. Journal of Geophysical Research 86, 8733–8743.

1355 Ingersoll, A. P., J., G. P., D., B., Vasavada, A. R., Galileo Imaging Team, Feb.
1356 2000. Moist convection as an energy source for the large-scale motions in
1357 Jupiter's atmosphere. Nature 403, 630–632.

1358 Irwin, P., Teanby, N., de Kok, R., Fletcher, L., Howett, C., Tsang, C., Wilson, C.,
1359 Calcutt, S., Nixon, C., Parrish, P., 2008. The NEMESIS planetary atmosphere
1360 radiative transfer and retrieval tool. Journal of Quantitative Spectroscopy and
1361 Radiative Transfer 109 (6), 1136–1150.

1362 Irwin, P. G. J., Dyudina, U., 2002. The Retrieval of Cloud Structure Maps in
1363 the Equatorial Region of Jupiter Using a Principal Component Analysis of
1364 Galileo/NIMS Data. Icarus 156, 52–63.

1365 Irwin, P. G. J., Weir, A. L., Smith, S. E., Taylor, F. W., Lambert, A. L., Calcutt,
1366 S. B., Cameron-Smith, P. J., Carlson, R. W., Baines, K., Orton, G. S., Drossart,

1367 P., Encrenaz, T., Roos-Serote, M., 1998. Cloud structure and atmospheric com-
1368 position of Jupiter retrieved from Galileo near-infrared mapping spectrometer
1369 real-time spectra. J. Geophys. Res. 103 (12), 23001–23022.

1370 Irwin, P. G. J., Weir, A. L., Taylor, F. W., Calcutt, S. B., Carlson, R. W., Feb.
1371 2001. The Origin of Belt/Zone Contrasts in the Atmosphere of Jupiter and Their
1372 Correlation with 5-μm Opacity. Icarus 149, 397–415.

1373 Irwin, P. J. G., Calcutt, S. B., Taylor, F. W., 1997. Radiative transfer models for
1374 galileo NIMS studies os the atmosphere of jupiter. Adv. Space Res. 19, 1149 –
1375 1158.

1376 Jacquinet-Husson, N., Scott, N. A., Chedin, A., Garceran, K., Armante, R.,
1377 Chursin, A. A., Barbe, A., Birk, M., Brown, L. R., Camy-Peyret, C., Claveau,
1378 C., Clerbaux, C., Coheur, P. F., Dana, V., Daumont, L., Debacker-Barilly, M. R.,
1379 Flaud, J. M., Goldman, A., Hamdouni, A., Hess, M., Jacquemart, D., Kopke, P.,
1380 Mandin, J. Y., Massie, S., Mikhailenko, S., Nemtchinov, V., Nikitin, A., Newn-
1381 ham, D., Perrin, A., Perevalov, V. I., Regalia-Jarlot, L., Rublev, A., Schreier,
1382 F., Schult, I., Smith, K. M., Tashkun, S. A., Teffo, J. L., Toth, R. A., Tyuterev,
1383 V. G., Vander Auwera, J., Varanasi, P., Wagner, G., Nov. 2005. The 2003 edi-
1384 tion of the GEISA/IASI spectroscopic database. Journal of Quantitative Spec-
1385 troscopy and Radiative Transfer 95, 429–467.

1386 Karkoschka, E., Tomasko, M., 2005. Saturn's vertical and latitudinal cloud struc-
1387 ture 1991 - 2004 from HST imaging in 30 filters. Icarus 179, 195–221.

1388 Karkoschka, E., Tomasko, M. G., 1992. Saturn's upper troposphere 1986-1989.
1389 Icarus 97, 161–181.

Karkoschka, E., Tomasko, M. G., 1993. Saturn's upper atmospheric hazes observed by the Hubble Space Telescope. Icarus 106, 428–441.

Kerola, D. X., Larson, H. P., Tomasko, M. G., 1997. Analysis of the Near-IR Spectrum of Saturn: A Comprehensive Radiative Transfer Model of Its Middle and Upper Troposphere. Icarus 127, 190–212.

Kim, J. H., Kim, S. J., Geballe, T. R., Kim, S. S., Brown, L. R., Dec. 2006. High-resolution spectroscopy of Saturn at 3 microns: CH_4, CH_3D, C_2H_2, C_2H_6, PH_3, clouds, and haze. Icarus 185, 476–486.

Kleiner, I., Tarrago, G., Cottaz, C., Sagui, L., Brown, L. R., Poynter, R. L., Pickett, H. M., Chen, P., Pearson, J. C., Sams, R. L., Blake, G. A., Matsuura, S., Nemtchinov, V., Varanasi, P., Fusina, L., Di Lonardo, G., 2003. NH_3 and PH_3 line parameters: the 2000 HITRAN update and new results. Journal of Quantitative Spectroscopy and Radiative Transfer 82, 293–312.

Lacis, A. A., Oinas, V., 1991. A description of the correlated-k distribution method for modelling nongray gaseous absorption, thermal emission, and multiple scattering in vertically inhomogeneous atmospheres. J. Geophys. Res. 96 (15), 9027–9064.

Larson, H. P., 1980. Infrared spectroscopic observations of the outer planets, their satellites, and the asteroids. Annual Review of Astronomy and Astrophysics 18, 43–75.

Lellouch, E., Bézard, B., Fouchet, T., Feuchtgruber, H., Encrenaz, T., de Graauw, T., 2001. The deuterium abundance in Jupiter and Saturn from ISO-SWS observations. Astron. Astrophys. 370, 610–622.

1413 Lewis, J. S., May 1969. The clouds of Jupiter and the NH_3-H_2O and NH_3-H_2S
1414 systems. Icarus 10, 365–378.

1415 Lian, Y., Showman, A. P., Apr. 2008. Deep jets on gas-giant planets. Icarus 194,
1416 597–615.

1417 Lian, Y., Showman, A. P., May 2010. Generation of equatorial jets by large-scale
1418 latent heating on the giant planets. Icarus 207, 373–393.

1419 Mandin, J., Aug. 1995. Line Positions and Intensities in the Vibrational System
1420 $2\nu2/\nu2 + \nu4/2\nu4/\nu1/\nu3$ of Arsine. Journal of Molecular Spectroscopy 172, 319–
1421 329.

1422 Marten, A., Rouan, D., Baluteau, J. P., Gautier, D., Conrath, B. J., Hanel, R. A.,
1423 Kunde, V., Samuelson, R., Chedin, A., Scott, N., May 1981. Study of the am-
1424 monia ice cloud layer in the Equatorial Region of Jupiter from the infrared
1425 interferometric experiment on Voyager. Icarus 46, 233–248.

1426 Martonchik, J. V., Orton, G. S., Appleby, J. F., Feb. 1984. Optical properties of
1427 NH3 ice from the far infrared to the near ultraviolet. Applied Optics 23, 541–
1428 547.

1429 McCord, T. B., Coradini, A., Hibbitts, C. A., Capaccioni, F., Hansen, G. B., Fi-
1430 lacchione, G., Clark, R. N., Cerroni, P., Brown, R. H., Baines, K. H., Bellucci,
1431 G., Bibring, J., Buratti, B. J., Bussoletti, E., Combes, M., Cruikshank, D. P.,
1432 Drossart, P., Formisano, V., Jaumann, R., Langevin, Y., Matson, D. L., Nelson,
1433 R. M., Nicholson, P. D., Sicardy, B., Sotin, C., Nov. 2004. Cassini VIMS ob-
1434 servations of the Galilean satellites including the VIMS calibration procedure.
1435 Icarus 172, 104–126.

1436 Momary, T. W., Baines, K. H., the Cassini/VIMS Science Team, Sep. 2006. The
1437 Zoology of Saturn: The Bizarre Features Unveiled by the 5 Micron Eyes of
1438 Cassini/VIMS. In: Bulletin of the American Astronomical Society. Vol. 38 of
1439 AAS/Division for Planetary Sciences Meeting Abstracts. p. 449.

1440 Nixon, C. A., Irwin, P. G. J., Calcutt, S. B., Taylor, F. W., Carlson, R. W., Mar.
1441 2001. Atmospheric Composition and Cloud Structure in Jovian 5-μm Hotspots
1442 from Analysis of Galileo NIMS Measurements. Icarus 150, 48–68.

1443 Noll, K. S., Geballe, T. R., Knacke, R. F., 1989. Arsine in Saturn and Jupiter.
1444 Astrophys. J. 338, L71–L74.

1445 Noll, K. S., Knacke, R. F., Geballe, T. R., Tokunaga, A. T., Oct. 1986. Detection
1446 of carbon monoxide in Saturn. ApJ Letters 309, L91–L94.

1447 Noll, K. S., Knacke, R. F., Geballe, T. R., Tokunaga, A. T., 1988. Evidence for
1448 germane in Saturn. Icarus 75, 409–422.

1449 Noll, K. S., Larson, H. P., 1990. The spectrum of Saturn from 1990–2230 cm^{-1}:
1450 abundances of AsH_3, CH_3D, CO, GeH_4, and PH_3. Icarus 89, 168–189.

1451 Noll, K. S., Larson, H. P., Geballe, T. R., Feb. 1990. The abundance of AsH3 in
1452 Jupiter. Icarus 83, 494–499.

1453 Orton, G. S., Baines, K. H., Cruikshank, D., Cuzzi, J. N., Krimigis, S. M., Miller,
1454 S., Lellouch, E., 2009. Review of Knowledge Prior to the Cassini-Huygens
1455 Mission and Concurrent Research, In: Saturn from Cassini-Huygens. Springer,
1456 Ch. 2, pp. 9–54.

1457 Orton, G. S., Serabyn, E., Lee, Y. T., 2000. Vertical Distribution of PH_3 in Saturn
1458 from Observations of Its 1-0 and 3-2 Rotational Lines. Icarus 146, 48–59.

1459 Pérez-Hoyos, S., Sánchez-Lavega, A., French, R. G., Rojas, J. F., 2005. Saturn's
1460 cloud structure and temporal evolution from ten years of Hubble Space Tele-
1461 scope images (1994-2003). Icarus 176, 155–174.

1462 Plass, G. N., Kattawar, G. W., Catchings, F. E., 1973. Matrix operator theory of
1463 radiative transfer. 1: Rayleigh scattering. Applied Optics 12, 314–329.

1464 Porco, C. C., Baker, E., Barbara, J., Beurle, K., Brahic, A., Burns, J. A., Charnoz,
1465 S., Cooper, N., Dawson, D. D., Del Genio, A. D., Denk, T., Dones, L., Dyud-
1466 ina, U., Evans, M. W., Giese, B., Grazier, K., Helfenstein, P., Ingersoll, A. P.,
1467 Jacobson, R. A., Johnson, T. V., McEwen, A., Murray, C. D., Neukum, G.,
1468 Owen, W. M., Perry, J., Roatsch, T., Spitale, J., Squyres, S., Thomas, P., Tis-
1469 careno, M., Turtle, E., Vasavada, A. R., Veverka, J., Wagner, R., West, R., 2005.
1470 Cassini Imaging Science: Initial Results on Saturn's Atmosphere. Science 307,
1471 1243–1247.

1472 Press, W. H., Flannery, B. P., Teukolsky, S. A., Vetterling, W. T., 1992. Numerical
1473 Recipes, 2nd Edition. Cambridge Univ. Press, Cambridge.

1474 Read, P. L., Conrath, B. J., Fletcher, L. N., Gierasch, P. J., Simon-Miller, A. A.,
1475 Zuchowski, L. C., Dec. 2009. Mapping potential vorticity dynamics on saturn:
1476 Zonal mean circulation from Cassini and Voyager data. Plan. & Space Sci. 57,
1477 1682–1698.

1478 Rodgers, C. D., 2000. Inverse Methods for Atmospheric Remote Sounding: The-
1479 ory and Practice. World Scientific.

Roos-Serote, M., Drossart, P., Encrenaz, T., Lellouch, E., Carlson, R. W., Baines, K. H., Kamp, L., Mehlman, R., Orton, G. S., Calcutt, S., Irwin, P., Taylor, F., Weir, A., Sep. 1998. Analysis of Jupiter North Equatorial Belt hot spots in the 4-5-μm range from Galileo/near-infrared mapping spectrometer observations: Measurements of cloud opacity, water, and ammonia. Journal of Geophysical Research 103, 23023–23042.

Rothman, L. S., Jacquemart, D., Barbe, A., Benner, D. C., Birk, M., Brown, L. R., Carleer, M. R., Chackerian, C., Chance, K., Coudert, L. H., Dana, V., Devi, V. M., Flaud, J. M., Gamache, R. R., Goldman, A., Hartmann, J. M., Jucks, K. W., Maki, A. G., Mandin, J. Y., Massie, S. T., Orphal, J., Perrin, A., Rinsland, C. P., Smith, M. A. H., Tennyson, J., Tolchenov, R. N., Toth, R. A., Vander Auwera, J., Varanasi, P., Wagner, G., Dec. 2005. The HITRAN 2004 molecular spectroscopic database. Journal of Quantitative Spectroscopy and Radiative Transfer 96, 139–204.

Salyk, C., Ingersoll, A., Lorre, J., Vasavada, A., Del Genio, A., 2006. Interaction between eddies and mean flow in Jupiter's atmosphere: Analysis of Cassini imaging data. Icarus 185 (2), 430–442.

Showman, A. P., de Pater, I., Mar. 2005. Dynamical implications of Jupiter's tropospheric ammonia abundance. Icarus 174, 192–204.

Showman, A. P., Ingersoll, A. P., Apr. 1998. Interpretation of Galileo Probe Data and Implications for Jupiter's Dry Downdrafts. Icarus 132, 205–220.

Sromovsky, L. A., Fry, P. M., Nov. 2010a. The source of 3-μm absorption in

Jupiter's clouds: Reanalysis of ISO observations using new NH_3 absorption models. Icarus 210, 211–229.

Sromovsky, L. A., Fry, P. M., Nov. 2010b. The source of widespread 3-μm absorption in Jupiter's clouds: Constraints from 2000 Cassini VIMS observations. Icarus 210, 230–257.

Stam, D. M., Banfield, D., Gierasch, P. J., Nicholson, P. D., Matthews, K., 2001. Near-IR Spectrophotometry of Saturnian Aerosols-Meridional and Vertical Distribution. Icarus 152, 407–422.

Tarrago, G., Lacome, Levy, A., Guelachvili, G., Bezard, B., Drossart, P., 1992. Phosphine spectrum at 4-5 μm : analysis and line-by-line simulation of 2v2, v2 + v4, v1, and v3 bands. Journal of molecular spectroscopy 154 (1), 30–42.

Temma, T., Chanover, N. J., Simon-Miller, A. A., Glenar, D. A., Hillman, J. J., Kuehn, D. M., 2005. Vertical structure modeling of Saturn's equatorial region using high spectral resolution imaging. Icarus 175, 464–489.

Terrile, R. J., Westphal, J. A., Feb. 1977. The vertical cloud structure of Jupiter from 5 micron measurements. Icarus 30, 274–281.

Vasavada, A. R., Hörst, S. M., Kennedy, M. R., Ingersoll, A. P., Porco, C. C., Del Genio, A. D., West, R. A., 2006. Cassini imaging of Saturn: Southern hemisphere winds and vortices. Journal of Geophysical Research (Planets) 111 (E10), 5004.

Weidenschilling, S. J., Lewis, J. S., 1973. Atmospheric and cloud structures of the jovian planets. Icarus 20, 465–476.

1524 Weisstein, E. W., Serabyn, E., 1996. Submillimeter Line Search in Jupiter and
1525 Saturn. Icarus 123, 23–36.

1526 West, R. A., Baines, K. H., Karkoschka, E., Sánchez-Lavega, A., 2009. Clouds
1527 and Aerosols in Saturn's Atmosphere, In: Saturn from Cassini-Huygens.
1528 Springer, Ch. 7, pp. 161–179.

1529 Westphal, J. A., Matthews, K., Terrile, R. J., Mar. 1974. Five-micron pictures of
1530 Jupiter. ApJ Letters 188, L111–L112.

1531 Yanamandra-Fisher, P. A., Orton, G. S., Fisher, B. M., Sanchez-Lavega, A., 2001.
1532 NOTE: Saturn's 5.2-μm Cold Spots: Unexpected Cloud Variability. Icarus 150,
1533 189–193.

Reference	q_{NH3}	Method
Courtin et al. (1984)	$(0.5 - 2.0) \times 10^{-4}$	Voyager/IRIS 180-300cm^{-1}
de Pater and Massie (1985)	5×10^{-4} at $p > 3$ bar	Very Large Array (VLA)
	3×10^{-5} at $p < 1.25$ bar	
Briggs and Sackett (1989)	$0.7 - 1.1 \times 10^{-4}$ at $p = 2$ bar	radio T_B
Grossman et al. (1989)	1.2×10^{-4} around condensation level	VLA
Noll and Larson (1990)	Upper limit 3×10^{-4}	5 μm spectra
de Graauw et al. (1997)	1.1×10^{-4} at $p = 1.2$ bar	ISO/SWS
Kerola et al. (1997)	Less than 1×10^{-9} at RC boundary	3 μm data
Orton et al. (2000)	1×10^{-4} with 3-4× uncertainty	Sub-mm PH_3 analysis
Burgdorf et al. (2004)	1×10^{-4}	ISO/LWS 96-101cm^{-1}
Kim et al. (2006)	6×10^{-8} at 460 mbar	3 μm data
	3×10^{-8} at 390 mbar	
Fletcher et al. (2009a)	$(3.3 \pm 0.3) \times 10^{-7}$ at 690 mbar	Cassini/CIRS Far-IR

Table 1: Vertical distribution of ammonia mole fraction from previous determinations.

Cube	Date	Start Time (UTC)	Stop Time (UTC)	Longitude	Range (km)	Phase (deg)
CM_1524383985	2006-Apr-22	07:29:22	08:04:01	128.1	2806258	114
CM_1524388848	2006-Apr-22	08:50:25	09:25:04	173.5	2793264	114
CM_1524393612	2006-Apr-22	10:09:49	10:44:28	218.1	2780503	114
CM_1524400806	2006-Apr-22	12:09:43	12:44:22	285.3	2760982	113
CM_1524403247	2006-Apr-22	12:50:24	13:25:03	308.1	2754393	113
CM_1524408018	2006-Apr-22	14:09:55	14:44:34	352.8	2741313	113
CM_1524412815	2006-Apr-22	15:29:52	16:04:31	37.6	2728032	113
CM_1524417617	2006-Apr-22	16:49:54	17:24:33	82.4	2714716	113

Table 2: VIMS-IR Cubes used in this study. The quoted longitude is for System III West at the start time of the observations.

Cloud Model	Description	Variables and Comments
I	Single Compact Cloud	p_b, τ_1
II	Two Compact Clouds	p_b, τ_1, τ_2 (Grey upper cloud fixed at 1.5 bar)
III	Single Extended Cloud	p_b, τ_1 (Extends to the tropopause)
IV	Compact Upper, Extended Deep	p_b, τ_1, τ_2 (Grey upper cloud fixed at 1.5 bar)
A	Grey cloud	Grey cross-section and $\omega_0 = 0.95$ across the full range; isotropic phase function
B	NH_3 ice	Martonchik et al. (1984)
C	NH_4SH	Ferraro et al. (1980)
D	Modified pseudo-NH_4SH	Refractive index $2.3 + 0.01i$ Nixon et al. (2001)
E	Updated NH_4SH	Howett et al. (2007)

Table 3: Summary of cloud models tested in this study, vertical structures I-IV, optical models A-E.

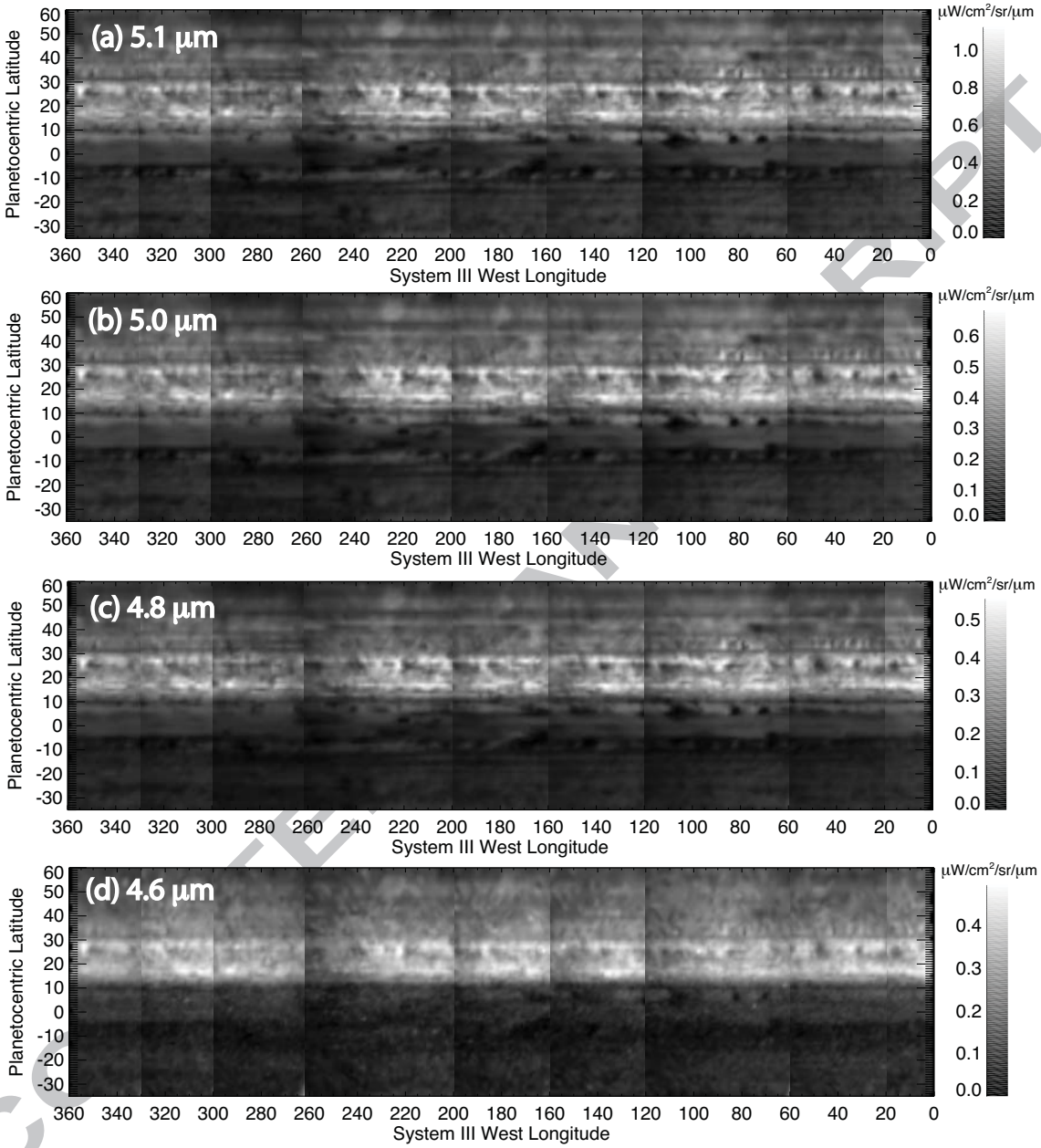

Figure 1:

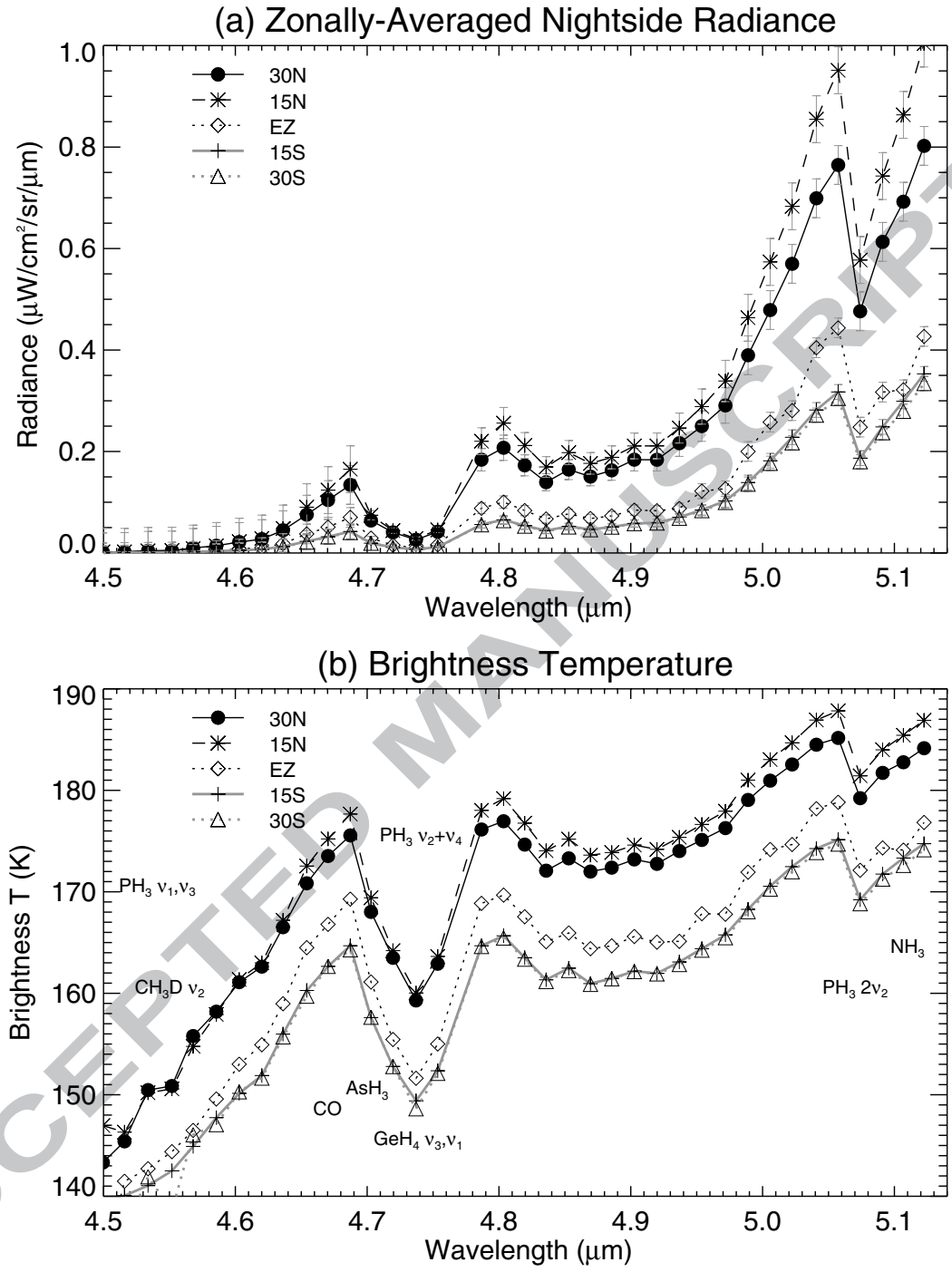

Figure 2:

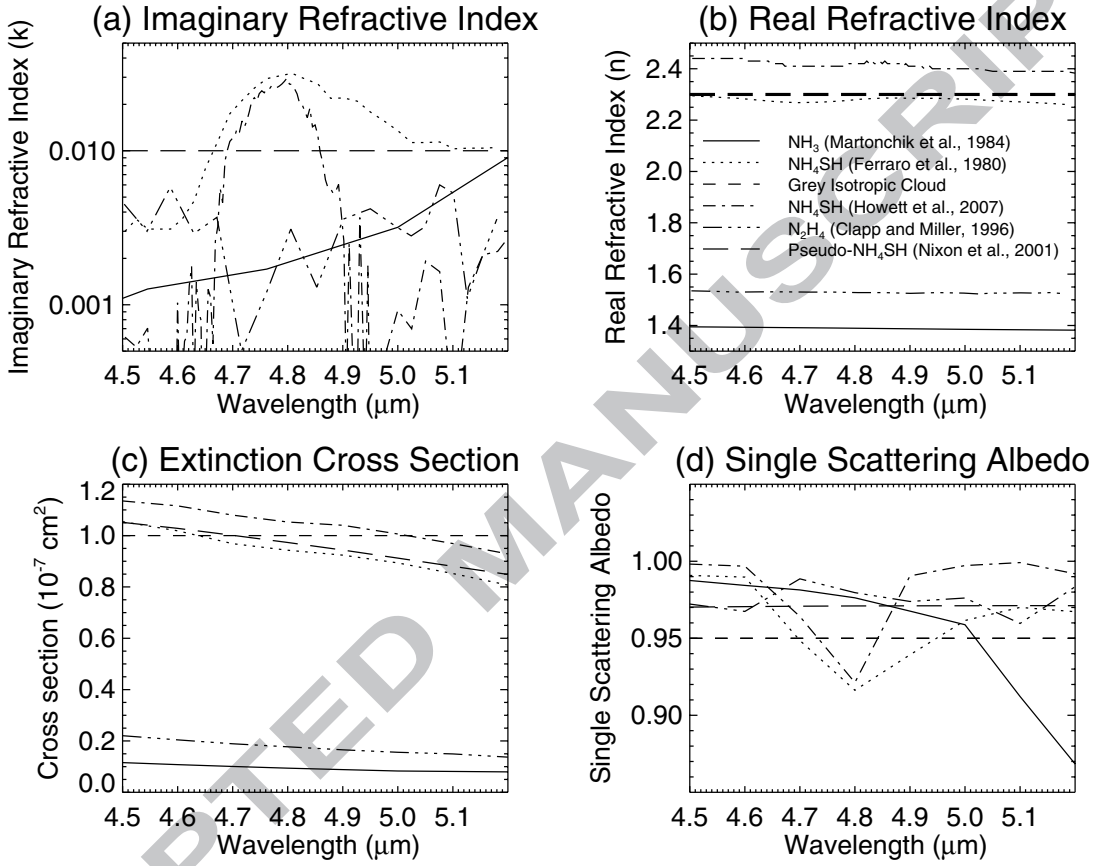

Figure 3:

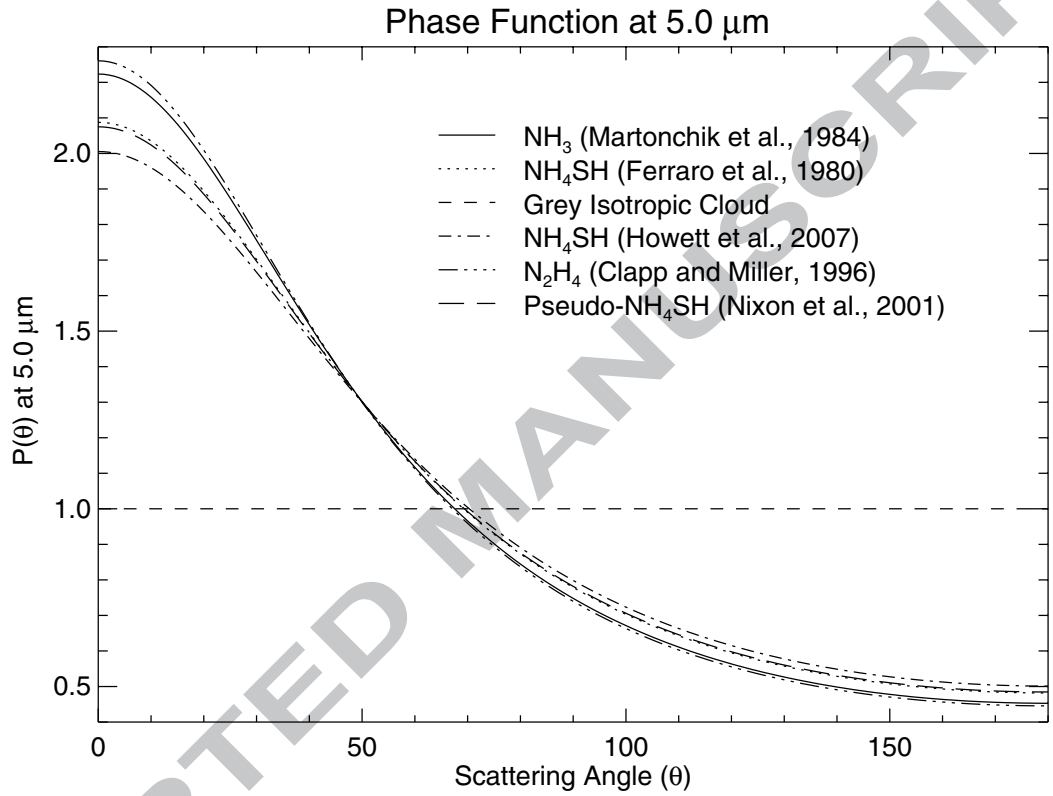

Figure 4:

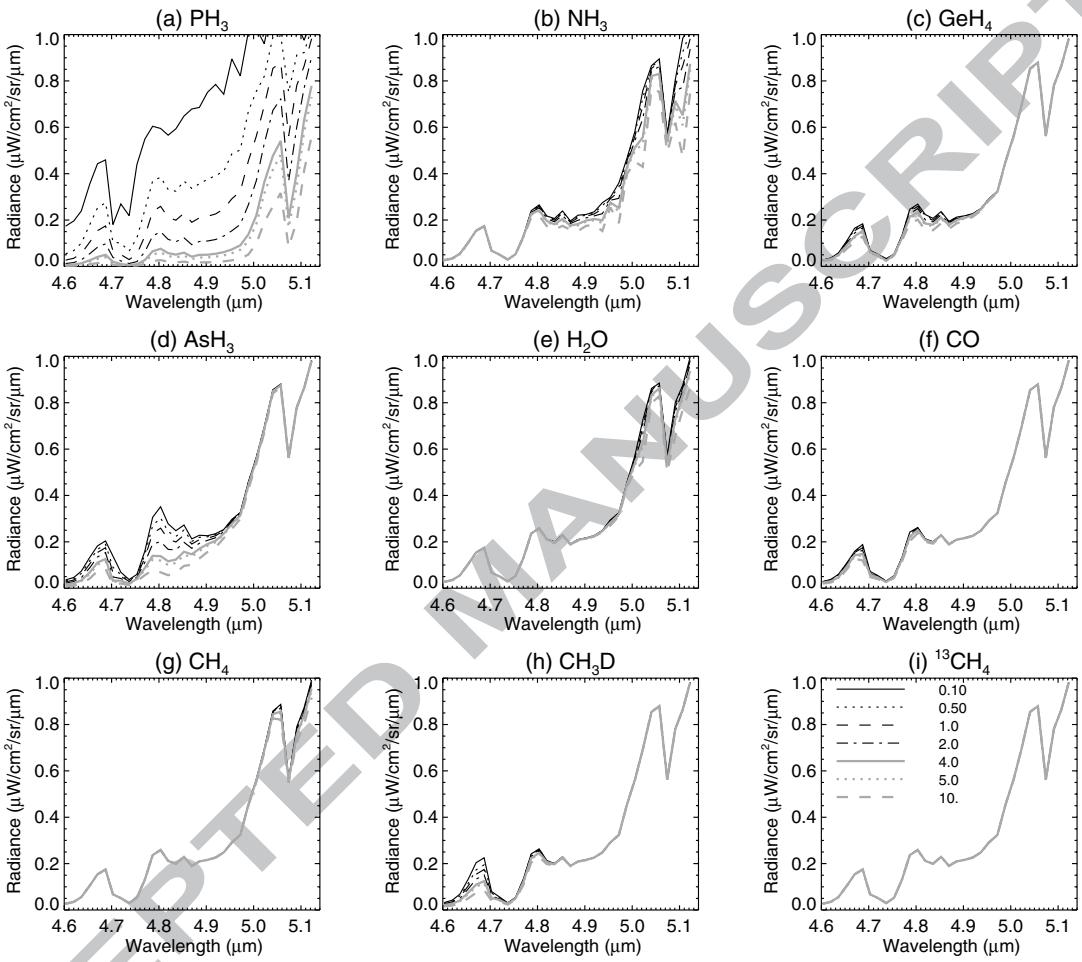

Figure 5:

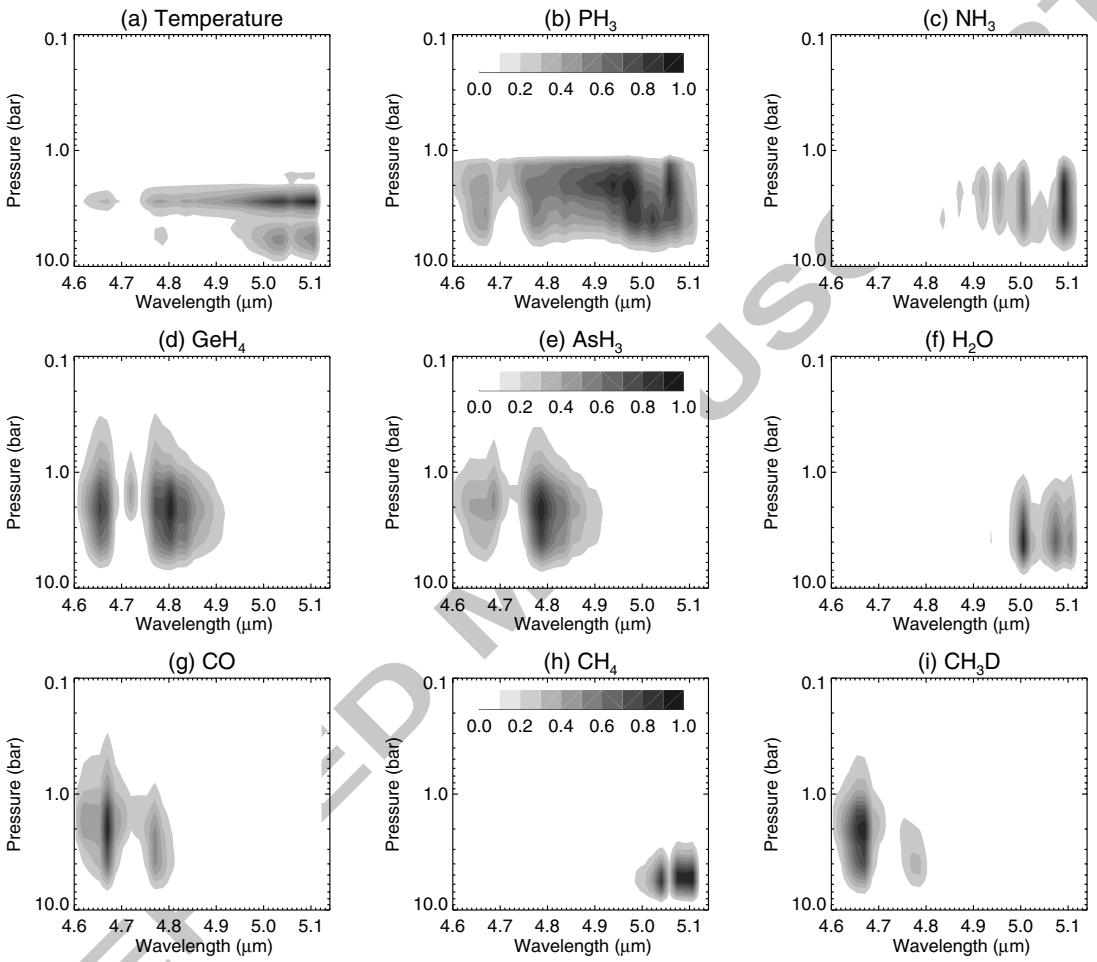

Figure 6:

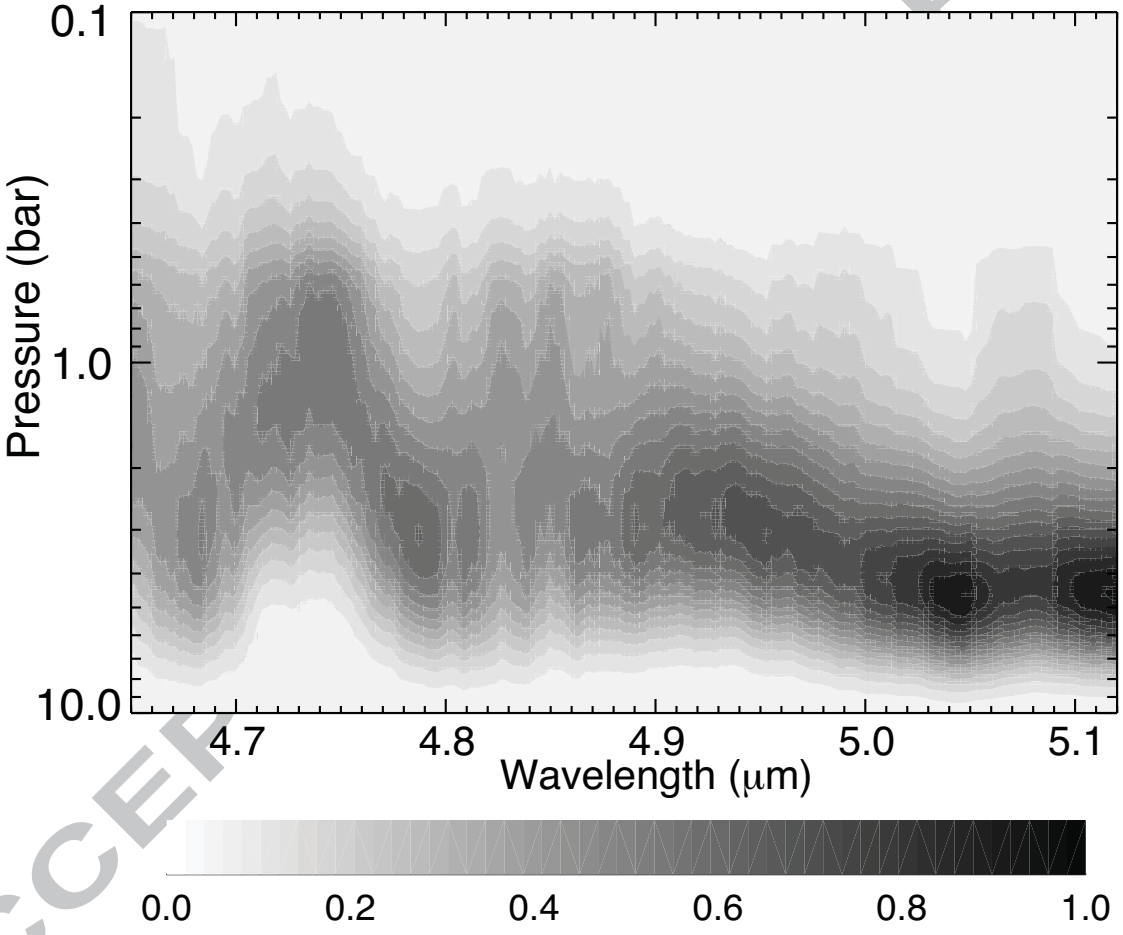

Figure 7:

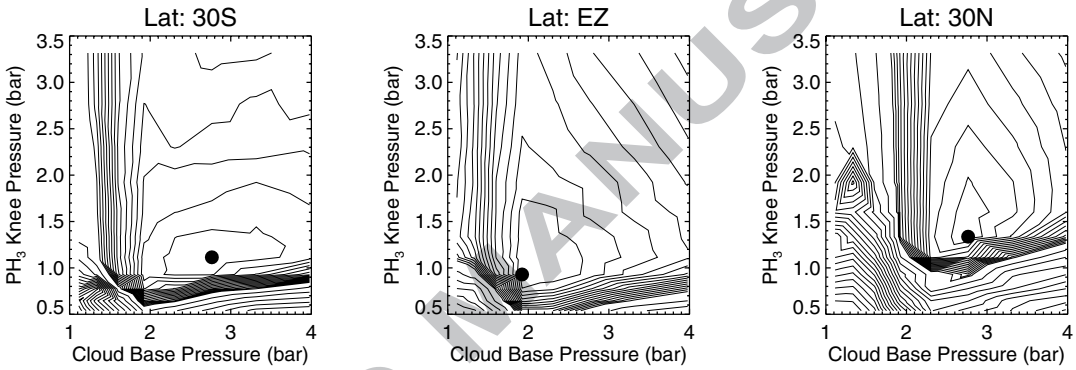

Figure 8:

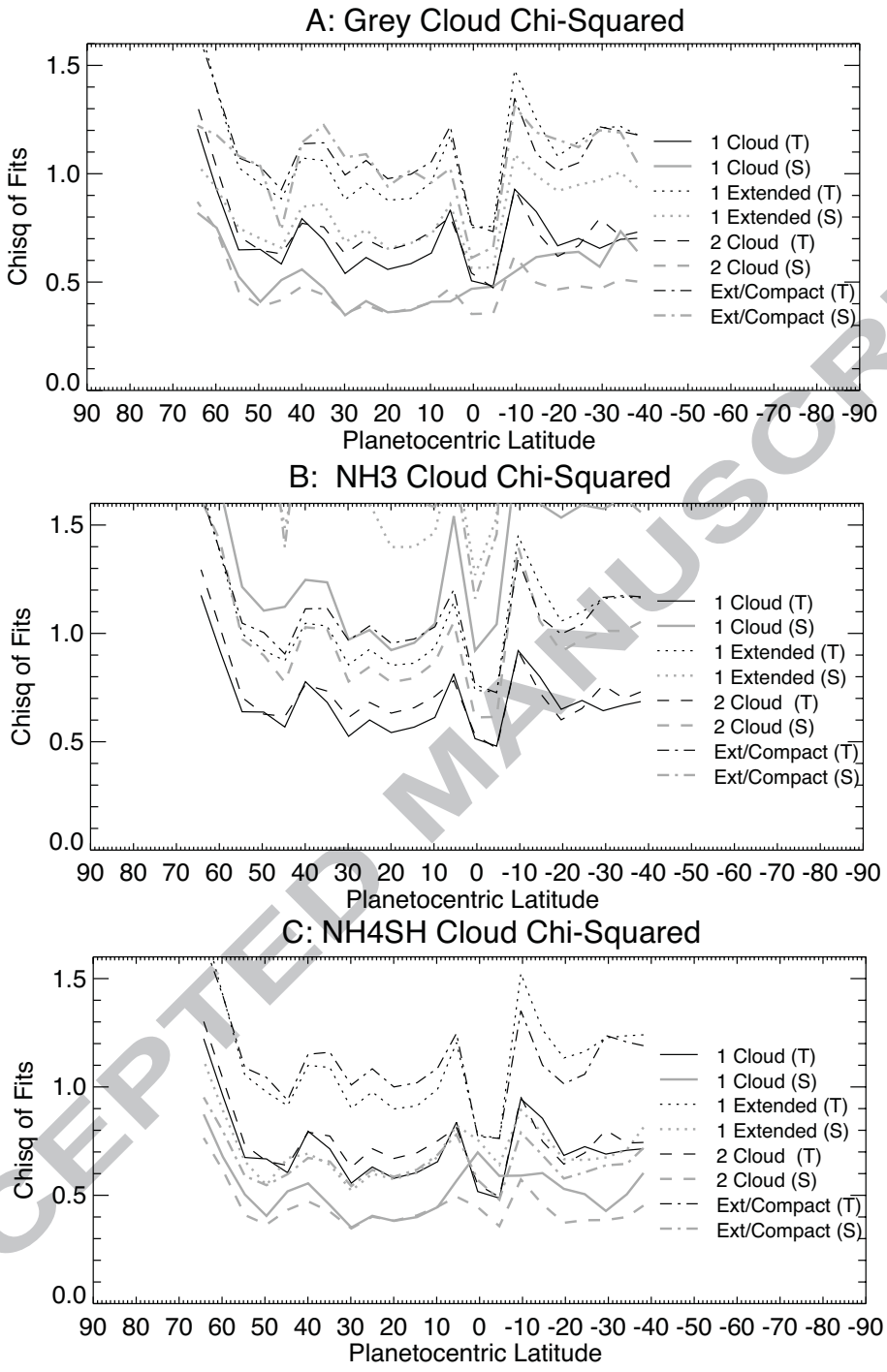

Figure 9:

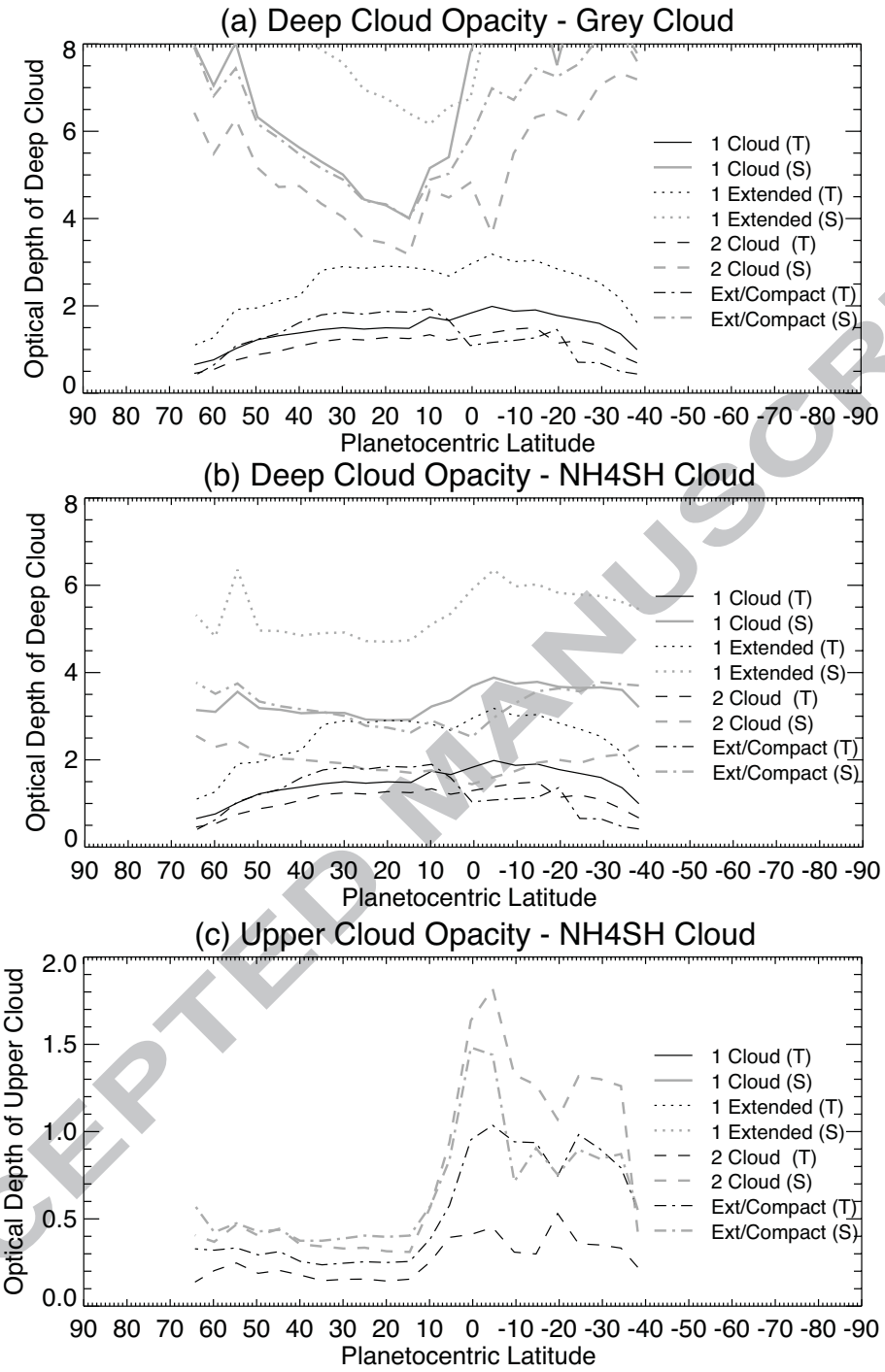

Figure 10:

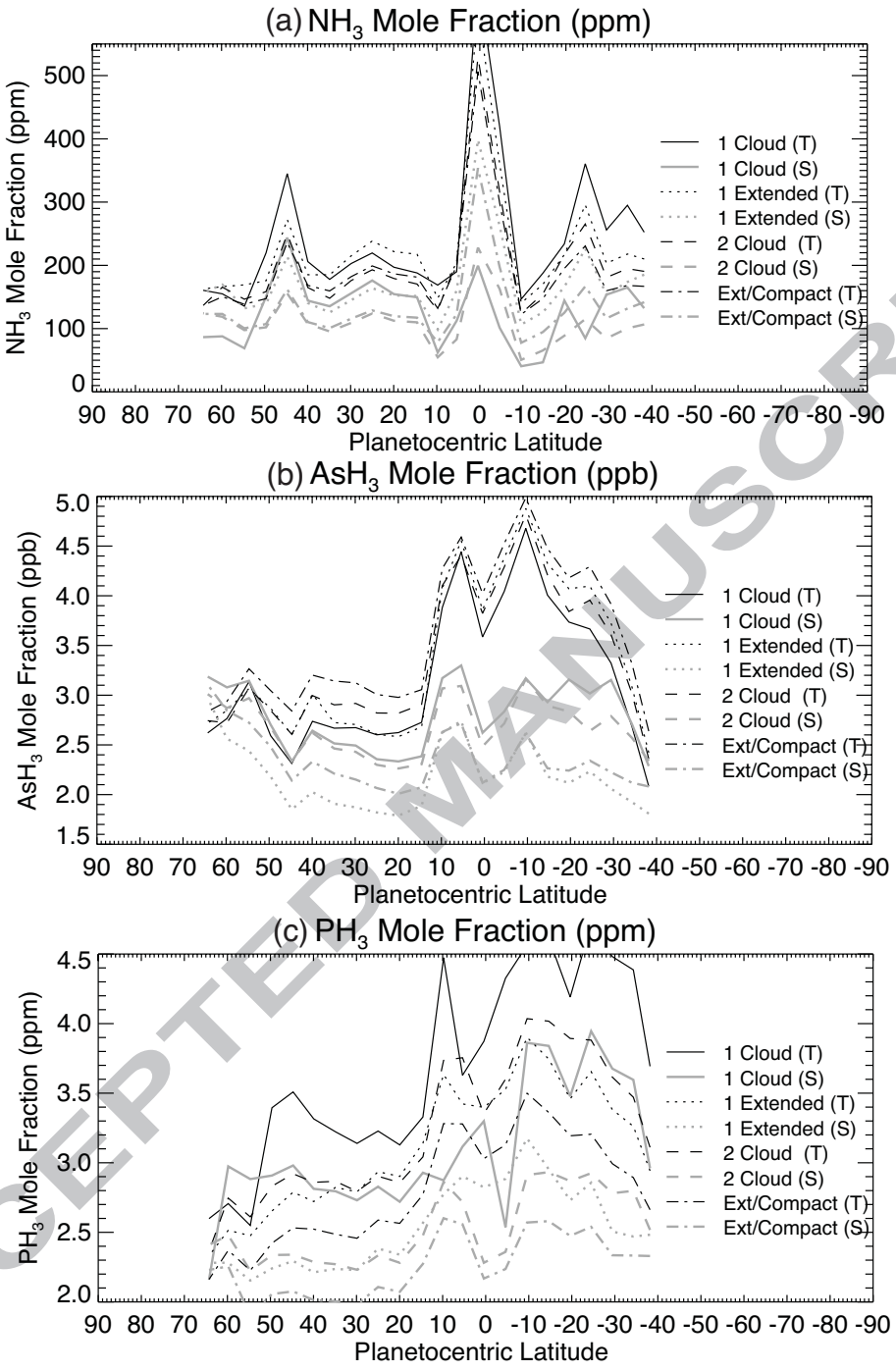

Figure 11:

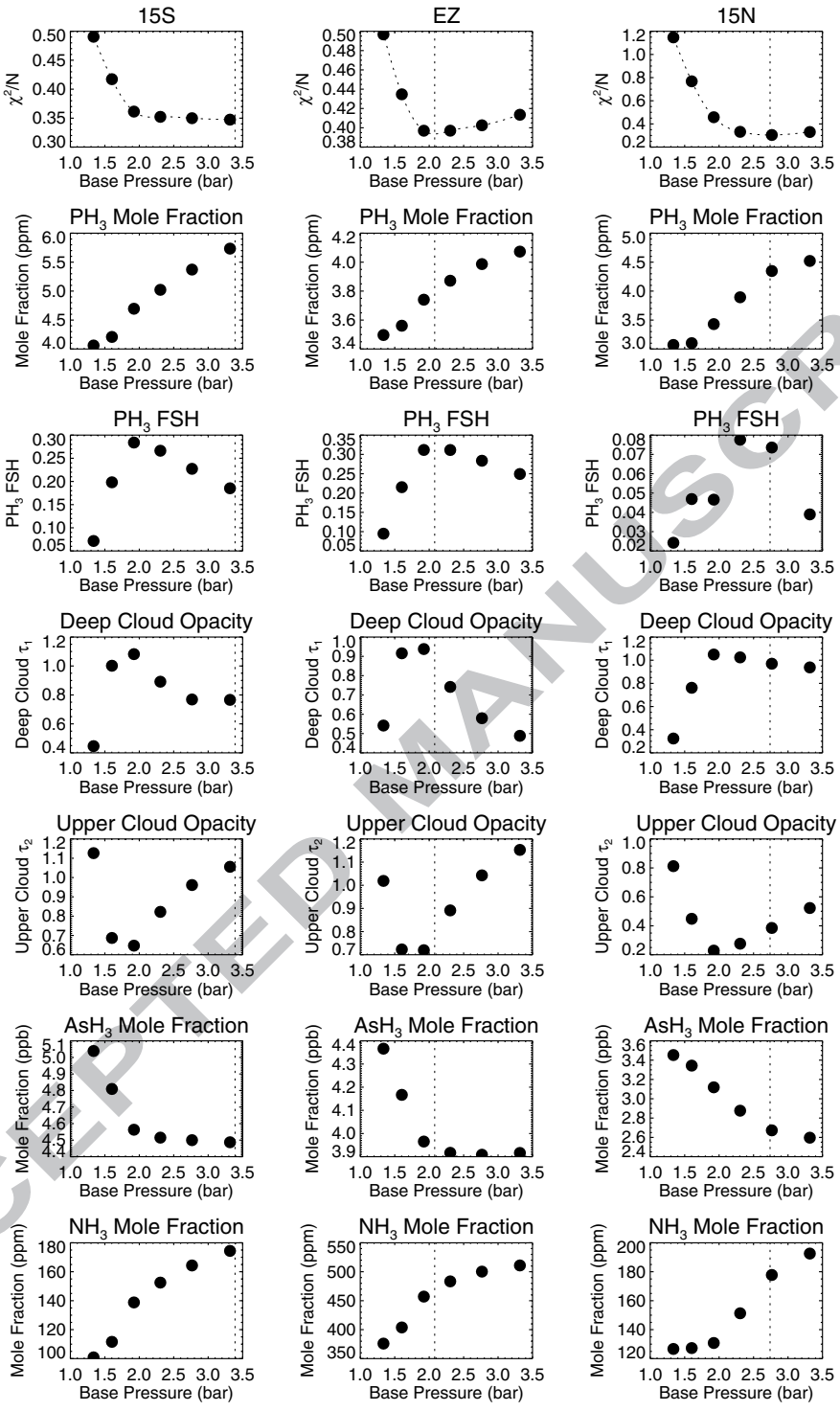

Figure 12:

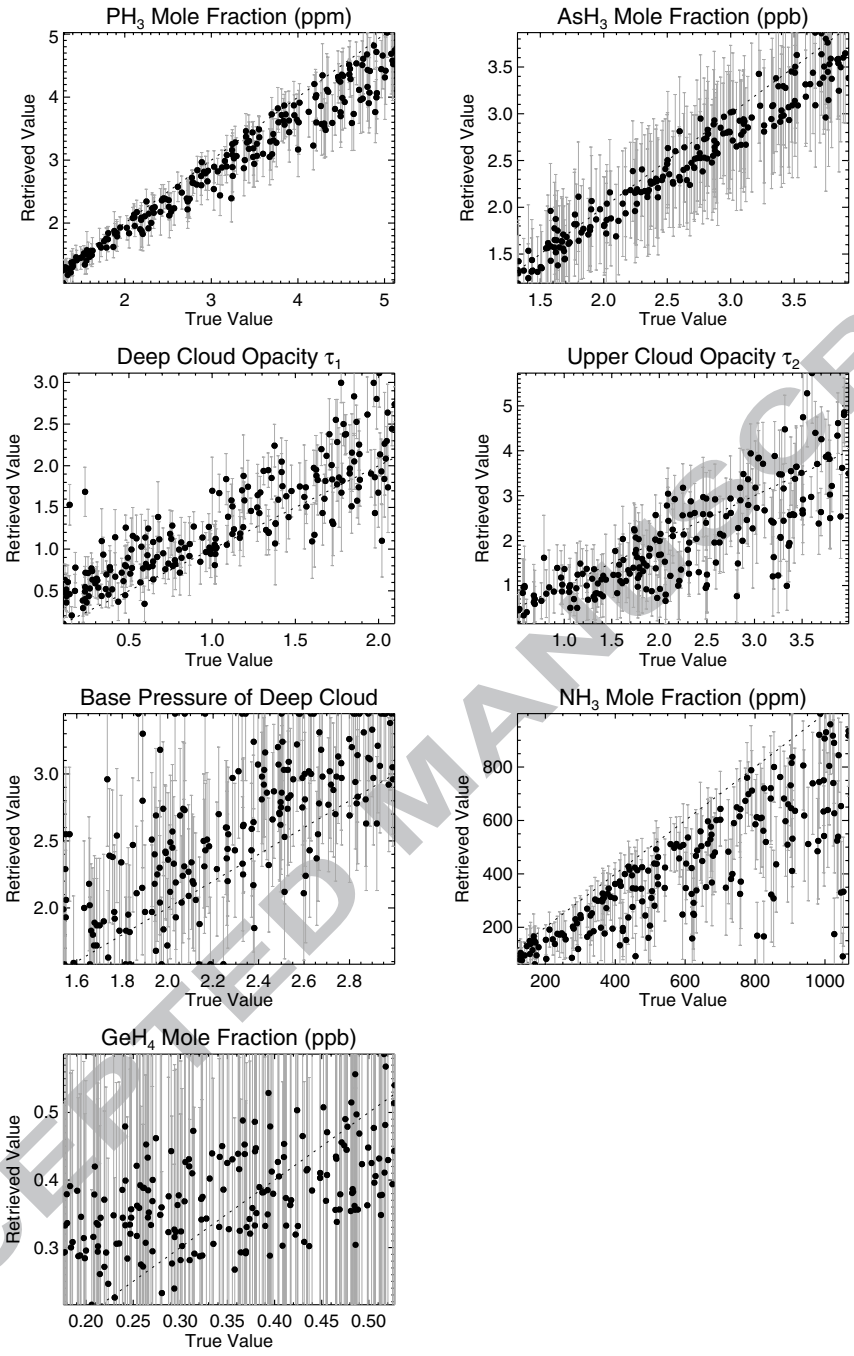

Figure 13:

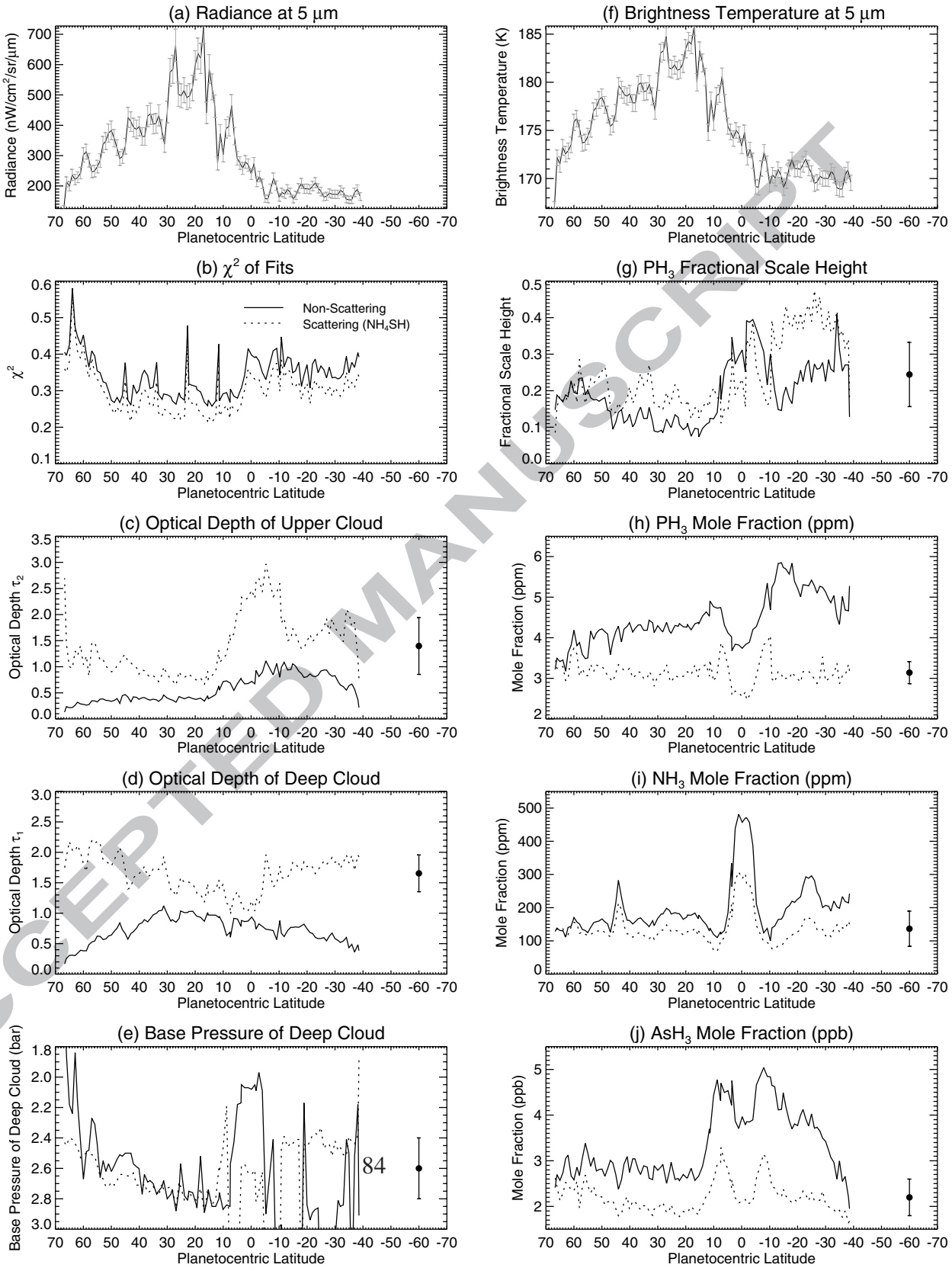

Figure 14:

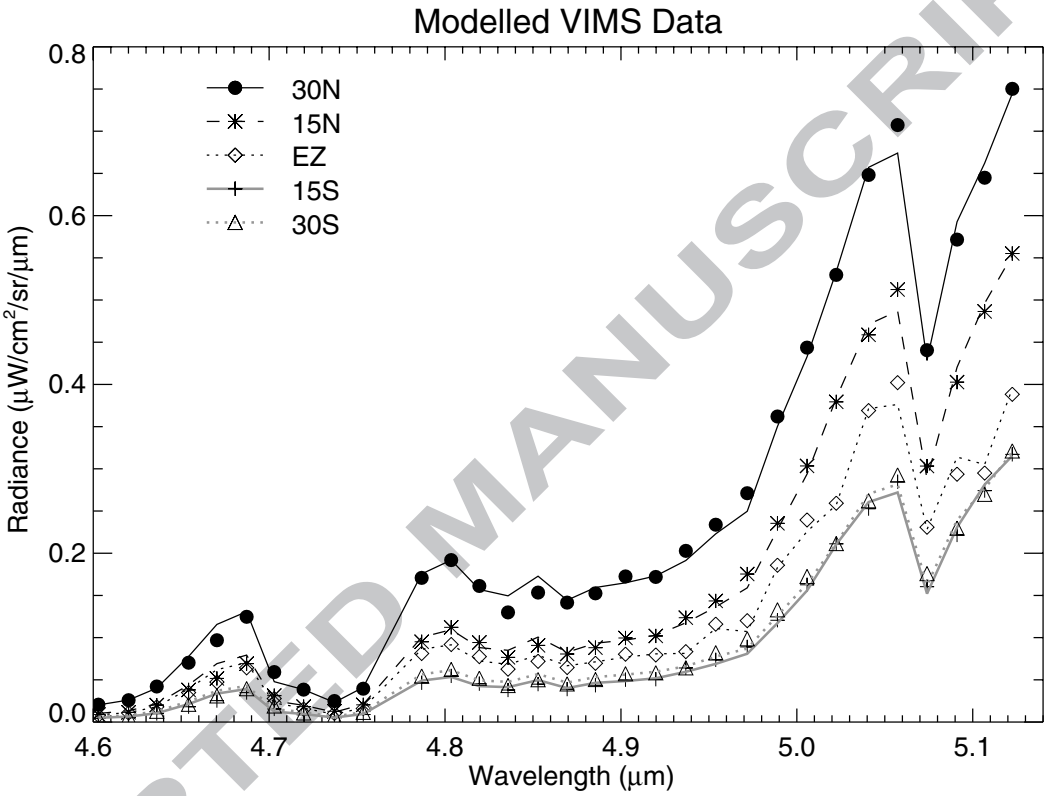

Figure 15:

Research Highlights

Saturn's Tropospheric Composition and Clouds from Cassini/VIMS 4.5-5.1 μm Nightside Spectroscopy

Fletcher et al.

- Saturn's spectrum contains a low-opacity window allowing us to study the atmosphere beneath the tropospheric hazes.
- Upwelling dredges ammonia, aerosols and phosphine to high altitudes at Saturn's equator.
- Strong extra-tropical upwelling and storms occur in broad regions near jets at 41N and 25S.
- Saturn's upper tropospheric hazes vary seasonally, whereas deep clouds are more uniform.
- Gases and clouds measured at 5 μm can be used to trace the circulation of Saturn's deep atmosphere.